



# Phenylethylammonium-formamidinium-methylammonium quasi-2D/3D tin wide-bandgap perovskite solar cell with improved efficiency and stability

SungWon Cho<sup>a,1</sup>, Padmini Pandey<sup>b,1</sup>, Jinwoo Park<sup>c</sup>, Tae-Woo Lee<sup>c,d</sup>, Hyungju Ahn<sup>e</sup>, Hyosung Choi<sup>f,\*</sup>, Dong-Won Kang<sup>a,b,\*</sup>

<sup>a</sup> Department of Smart City, Chung-Ang University, 84 Heukseok-ro, Dongjak-gu, Seoul 06974, Republic of Korea

<sup>b</sup> Department of Energy Systems Engineering, Chung-Ang University, 84 Heukseok-ro, Dongjak-gu, Seoul 06974, Republic of Korea

<sup>c</sup> Department of Materials Science and Engineering, Seoul National University, 1 Gwanak-ro, Gwanak-gu, Seoul 08826, Republic of Korea

<sup>d</sup> Institute of Engineering Research, Research Institute of Advanced Materials, Soft Foundry, School of Chemical and Biological Engineering, Seoul National University, 1 Gwanak-ro, Gwanak-gu, Seoul 08826, Republic of Korea

<sup>e</sup> Pohang Accelerator Laboratory, POSTECH, Pohang 37673, Republic of Korea

<sup>f</sup> Department of Chemistry, Research Institute for Convergence of Basic Science, and Research Institute for Natural Science, Hanyang University, Seoul 04763, Republic of Korea

## ARTICLE INFO

### Keywords:

Wide bandgap  
Sn perovskite  
Phenylethylammonium  
2D/3D mixed perovskite

## ABSTRACT

Wide bandgap (WBG) Sn perovskite solar cells (PSCs) efficiency enhancement is another sought after field and to resolve the issues related to fast crystallization, trap density and moisture induced oxidation of  $\text{Sn}^{2+}$  state in Sn perovskite, we endeavor the benefits of substituting hydrophobic phenylethylammonium ( $\text{PEA}^+$ ) cation into WBG  $\text{PEA}_x\text{FA}_{0.75}\text{MA}_{0.25-x}\text{SnI}_2\text{Br}$  through compositional engineering. We have realized that  $\text{PEA}^+$  substitution in WBG Sn perovskite led to form 2D/3D mixed perovskite and execute preferential orientation of 3D perovskite planes with controlled crystallinity. Our observation suggests that 2D perovskite phase here helps in merging the grain boundaries and reduce the rate of moisture penetration which ultimately controlled further oxidation of  $\text{Sn}^{2+}$ . Also, the substitution of  $\text{PEA}^+$  in WBG Sn perovskite helps in modulating the band energies and aids to efficient electron injection from perovskite to transport layer. Compared to the 3D counterpart, 2D/3D perovskite exhibits slow lifetime decay ( $\tau_{\text{avg}} = 1.25$  ns), suppressed trap state density ( $1.7 \times 10^{16} \text{ cm}^{-3}$ ), improved band alignment with slower carrier recombination ( $\tau = 1217$   $\mu\text{s}$ ) and efficient charge extraction. As compared to  $\text{FASnI}_2\text{Br}$  (PCE of 2.38%) and  $\text{FA}_{0.75}\text{MA}_{0.25}\text{SnI}_2\text{Br}$  (PCE of 3.66%), our champion device PCE of 7.96% (Certified PCE of 7.84%) with  $J_{\text{sc}}$  of  $16.89 \text{ mA cm}^{-2}$ ,  $V_{\text{oc}}$  of 0.67 V and FF of 70.36% was achieved for  $\text{PEA}_{0.15}\text{FA}_{0.75}\text{MA}_{0.10}\text{SnI}_2\text{Br}$ , which is the highest PCE till date with compositional engineering strategy. The device kept under  $\text{N}_2$  atmosphere retained nearly original PCE after almost 1500 hrs and air stability of 300 hrs without encapsulation, indicating excellent stability.

## 1. Introduction

Over the past decades, the ways toward utilizing renewable energies especially the solar energy are growing tremendously [1,2]. Competing with silicon technology, hybrid halide perovskites (HHPs) have been extensively used as efficient photo-absorbers and with continuous

research and development, they reached to the certified power conversion efficiency (PCE) more than 25% [3] till date. Such tremendous improvements in device efficiency enhancement over the years have been developed in HHPs due to the existence of extraordinary physical and optoelectronic properties, ease fabrication processes, compositional engineering for bandgap tuning and stability [4–7]. Either the silicon

\* Corresponding authors at: Department of Energy Systems Engineering, Chung-Ang University, 84 Heukseok-ro, Dongjak-gu, Seoul 06974, Republic of Korea (D.-W. Kang). Department of Chemistry, Research Institute for Convergence of Basic Science, and Research Institute for Natural Science, Hanyang University, Seoul 04763, Republic of Korea (H. Choi).

E-mail addresses: [hschoi202@hanyang.ac.kr](mailto:hschoi202@hanyang.ac.kr) (H. Choi), [kangdwn@cau.ac.kr](mailto:kangdwn@cau.ac.kr) (D.-W. Kang).

<sup>1</sup> Contributed equally.

<https://doi.org/10.1016/j.cej.2022.137388>

Received 15 March 2022; Received in revised form 1 June 2022; Accepted 3 June 2022

Available online 6 June 2022

1385-8947/© 2022 Elsevier B.V. All rights reserved.

photovoltaic (PV) or HHP solar cells can achieve excellent efficiencies in single junction devices, however most of the spectral radiation loss limits their performances. However, they are incapable to avoid excess thermalization loss and cannot utilize photons with energy lower than the bandgap of photo-absorber and hence suffers from limited optical response. However, PV technology evolves further to exploit maximum solar radiation with tandem solar cells (TSCs) which utilizes maximum radiations in lower as well as higher wavelength regions by stacking multiple cells as front and rear sub-cells in stacks [8,9]. Progress in tandem device technology is highly beneficial to harness maximum photons in the broad spectral range and compared to single junction solar cells, the TSC technology is useful to achieve enhanced PCEs. In TSCs photons with lower wavelengths get absorbed by front wide bandgap sub-cell (WBG in the range of 1.6–2.3 eV), whereas photons of longer wavelengths get absorbed by rear narrow-bandgap (NBG, in the range of 1–1.5 eV) sub-cell [8,10,11] which permits the harnessing of maximum photons. Several efforts have been made by pioneering research groups to implement HHPs in TSCs [12,13]. Pb perovskites exhibit extraordinary properties, the uniqueness in electronic configuration  $6s^2 6p^0$ , and strong spin-orbit coupling are responsible for the tremendous growth for developing high efficiency perovskite solar cells (PSCs) [14]. In both 2-terminal (2T) and 4-terminal (4T) TSCs, WBG front sub-cells are responsible to reach high  $V_{oc}$  and at present it's a part of extensive investigation to develop high quality WBG photo absorbers. Selecting photo-absorber with appropriate bandgap needs to be accurately followed to maximize  $J_{sc}$  in 2T-TSCs, whereas in 4T-TSCs the overall power is the sum of PCEs of sub-cells and hence a photo-absorber in a wide range of bandgaps can be selected as front sub-cell [15]. The theoretical PCE limit of 40% may get achieved by precisely choosing suitable narrow and wide band gap materials [11], in this line Pb-HHPs with tunable properties can be easily stacked in perovskite/Si, perovskite/CIGS and all-perovskite TSCs [16–18]. Though loaded with such tremendous properties, the commercialization of Pb PSCs is still a challenge due to the existence of Pb-toxicity and instability which are considered as major drawbacks towards its commercialization [19]. Although several efforts have been made till date to reduce the leakage and instability issues by adopting recycling and encapsulation strategies [20,21], perhaps these approaches are not appropriate to completely alleviate the risk of Pb leakage. The toxicity issue is a serious concern including Pb poisoning which affect human health, pollute environment at an extreme level. Pb have the tendency to mimic other elements such as Zn, Ca, Fe etc. and accumulate in the nervous system with neurological disorders, genetical damage, carcinogenic, and so on [19,22]. With constant efforts in developing low toxic perovskites, the partial replacement of Pb with Sn seems quite successful, which tends to bandgap reduction, hence such low toxic materials have been utilized as narrow bandgap (NBG) photo-absorbers in TSCs [23,24]. Even the complete replacement of Pb with Sn in HHPs reaches to respectable PCEs in NBG PSCs with several efforts till date [25]. Nevertheless, to solve the issue of Pb toxicity and utilizing maximum solar spectral range, there is an urgent demand to develop wide bandgap (WBG) Pb-free perovskites with enhanced efficiencies that can be suitable as front sub-cells for Pb-free all-perovskite TSCs. Although Sn perovskites can be a suitable replacement to Pb, however due to more active s electrons, high Lewis's acidity and high energy of Sn-I bonds, Sn perovskites suffer from certain issues such as uncontrolled crystallization, defect formation and poor band alignment in device [26]. WBG absorbers are majorly participate in  $V_{oc}$  enhancement in TSCs, hence the technical challenge in WBG Sn perovskites is to develop photo absorber which can have better band alignments with the charge transport layers and needs to develop such strategies through which the  $V_{oc}$  deficit can be reduced. In NBG Sn PSCs, the highest PCE has been reached to 14.8% [27], whereas WBG Sn PSCs are still lagging in the performance with almost PCE  $\sim$ 11.17% [28] till date. Non-radiative recombination which originates through the formation of trap densities is responsible for  $V_{oc}$  deficit. Intrinsic defects form in mixed halide WBG perovskites during nucleation and growth of

perovskite crystal and depend upon the processing conditions, compositional engineering, and stoichiometry of the precursor in the solution. Compositional engineering in WBG perovskites is very critical step, since bandgap tuning can be achieved by altering halide ion in perovskites. The mixed halide perovskites suffer from light induced phase segregation and results in the formation of iodine rich phase with lower bandgap ultimately responsible for  $V_{oc}$  deficit in WBG perovskites [29,30].

In this line various WBG Sn-based all-inorganic and HHPs have been explored from past few years to enhance the PCEs. The PCE enhancement from 1.7% [31] to 11.17% in 2021 [28] has been achieved for FASnI<sub>2</sub>Br WBG Sn PSCs. Constant efforts have been made in past few years to enhance device efficiency in WBG Sn perovskites through crystal growth control by annealing temperature optimization, compositional engineering to stabilize Sn<sup>2+</sup> state, trap densities reduction by adding SnF<sub>2</sub>, GeI<sub>2</sub>, EDAI, GAI and interfacial engineering by adding small molecules at perovskite/HTL interface [32–35]. Notably the highest PCE achieved in WBG Sn PSC was accomplished with multiple strategies of material engineering (PCE  $\sim$ 7.6%) as well as interfacial modification with KSCN (PCE  $\sim$ 11.17%) [28]. Some of the major issues include fast crystallization with non-uniformity results in trap densities, moisture penetration from surface and grain boundaries tend to film degradation, oxidation of Sn<sup>2+</sup> to Sn<sup>4+</sup> and so on [36]. Over the years to overcome these issues for PCE enhancement, a desirable route is to mitigate non-radiative recombination and associated trap densities via surface and bulk defect passivation which can be achieved through compositional modifications in perovskite or surface treatments. In addition, the issue associated to the instability in WBG Sn perovskites put another barrier in device efficiency enhancement which collectively considered to be the major challenges in this field. Introducing organic cation in HHPs which are hydrophobic in nature can effectively reduce the rate of moisture penetration, helps in passivating perovskite grain boundaries, reduce trap densities, and enhance perovskite stability. Different strategies have been previously adopted to get benefits of organic cations in Pb based HHPs and Sn based NBG perovskites, through compositional engineering results in formation of 2D/3D heterostructures or even surface treatment leads to the development of 2D layer over 3D perovskites [37–40]. In WBG Sn PSC, there were no successful research on improving the internal characteristics of WBG Sn perovskite using PEA. There is only one study that deals with PEA substitution in CsSnI<sub>2</sub>Br however, they have reported very low PCE (0.71%) in CsSnI<sub>2</sub>Br-P and the report did not successfully verify the PEA effect [41]. To develop high efficiency Pb-free TSCs it is crucial to focus equally on WBG (1.6 eV) Sn PSCs.

With perovskite compositional engineering, we focused on sorting various issues associated such as defect passivation, bandgap tuning for efficient charge extraction and stability improvement which collectively helps in increasing the PCE in WBG Sn perovskites. Herein we endeavored the incorporation of phenylethylammonium (PEA<sup>+</sup>) cation into mixed-cation mixed-halide WBG ( $E_g \sim$ 1.66 eV) Sn perovskite to improve the perovskite film uniformity and stability of the device. We are the first to achieve the highest PCE with compositional engineering strategy in WBG Sn perovskite, the highest efficiency achieved here is 7.96% (Certified PCE of 7.84%) for the champion device in p-i-n architecture which retained almost equivalent PCE as of initial performance for almost 1500 hrs with excellent stability (without encapsulation kept under N<sub>2</sub> filled glovebox for monitoring and measured in ambient atmospheric conditions). We further discussed how the introduction of PEA<sup>+</sup> cation in perovskite precursor during compositional engineering forms quasi-2D/3D mixed perovskite and helps to improve the film uniformity, device stability and efficiency. PEA<sup>+</sup> cation substitution forms quasi 2D perovskite traced through XRD and FE-SEM analysis, it helps to improve crystallinity and preferential orientation of the 3D perovskite grains (as observed from GIWAXS). The grain boundary passivation in 2D/3D mixed perovskite film as observed through FE-SEM helps in reduced non-radiative recombination. The existence of

hydrophobic  $\text{PEA}^+$  cation reduce the rate of moisture penetration as well in 2D/3D WBG Sn perovskite which suppress further oxidation of  $\text{Sn}^{2+}$ . More observations revealed that the existence of 2D perovskite aids to quantum confinement and executes bandgap tuning, additionally the upshift of conduction band in 2D/3D mixed perovskite helps in better alignment of energy levels in the device, which offered efficient charge injection from perovskite to electron transport layer. Notably, the improved film uniformity suppressed the trap density states and non-radiative recombination processes. Also, the proposed method executed faster charge injections, and hence collectively supported in achieving enhanced PCE in WBG Sn PSC with excellent stability. We expect that new interfacial strategies for appropriate band alignments and overcoming  $V_{oc}$  deficit are much needed to promote it to next level at technological grounds and develop more eco-friendly single junction and TSCs.

## 2. Results and discussion

We tuned the ratio of  $\text{PEA}^+$  with respect to  $\text{MA}^+$  by fixing  $\text{FA}^+$  ratio in the precursor composition of  $\text{PEA}_x\text{FA}_{0.75}\text{MA}_{0.25-x}\text{SnI}_2\text{Br}$ , where  $x = 0.05, 0.10, 0.15$  and  $0.20$ , details related to film and device fabrication is

provided in supporting information (SI). To simply differentiate all the cases following codes will be used throughout  $\text{FASnI}_2\text{Br}$  (FA),  $\text{FA}_{0.75}\text{MA}_{0.25}\text{SnI}_2\text{Br}$  ( $\text{FA}_{0.75}\text{MA}_{0.25}$ ),  $\text{PEA}_{0.05}\text{FA}_{0.75}\text{MA}_{0.20}\text{SnI}_2\text{Br}$  ( $\text{PEA}_{0.05}\text{FA}_{0.75}\text{MA}_{0.20}$ ),  $\text{PEA}_{0.10}\text{FA}_{0.75}\text{MA}_{0.15}\text{SnI}_2\text{Br}$  ( $\text{PEA}_{0.10}\text{FA}_{0.75}\text{MA}_{0.15}$ ),  $\text{PEA}_{0.15}\text{FA}_{0.75}\text{MA}_{0.10}\text{SnI}_2\text{Br}$  ( $\text{PEA}_{0.15}\text{FA}_{0.75}\text{MA}_{0.10}$ ) and  $\text{PEA}_{0.20}\text{FA}_{0.75}\text{MA}_{0.05}\text{SnI}_2\text{Br}$  ( $\text{PEA}_{0.20}\text{FA}_{0.75}\text{MA}_{0.05}$ ). To understand the role of  $\text{PEA}^+$  cation in WBG Sn perovskite, we investigated how  $\text{PEA}^+$  cation addition helps to control morphology through FE-SEM measurement. As shown in Fig. 1(a-b), the FE-SEM micrograph and cross-sectional image for FA perovskite, the developed grain size is very random and smaller, with several pin holes which reveals poor film quality. To further control the film morphology, as per the previous reports substitution of certain ratio of  $\text{MA}^+$  in halide perovskite controls the grain growth [42]. With addition of  $\text{MA}^+$  in  $\text{FASnI}_2\text{Br}$  (namely  $\text{FA}_{0.75}\text{MA}_{0.25}$ ) the crystal growth comparatively improved but not much variation was observed, however few pinholes and sharp grain boundaries can be seen from FE-SEM top view and cross-sectional image (Fig. 1(c-d)). With substitution of  $\text{PEA}^+$  cation in  $\text{FA}_{0.75}\text{MA}_{0.25}$  perovskite ( $\text{PEA}_x\text{FA}_{0.75}\text{MA}_{0.25-x}\text{SnI}_2\text{Br}$ , where  $x = 0.05, 0.10, 0.15$  and  $0.20$ ), as shown in Fig. 1(e-f) for  $\text{PEA}_{0.15}\text{FA}_{0.75}\text{MA}_{0.10}$  FE-SEM micrograph, leads to the formation of uniform perovskite film with negligible pinholes. It

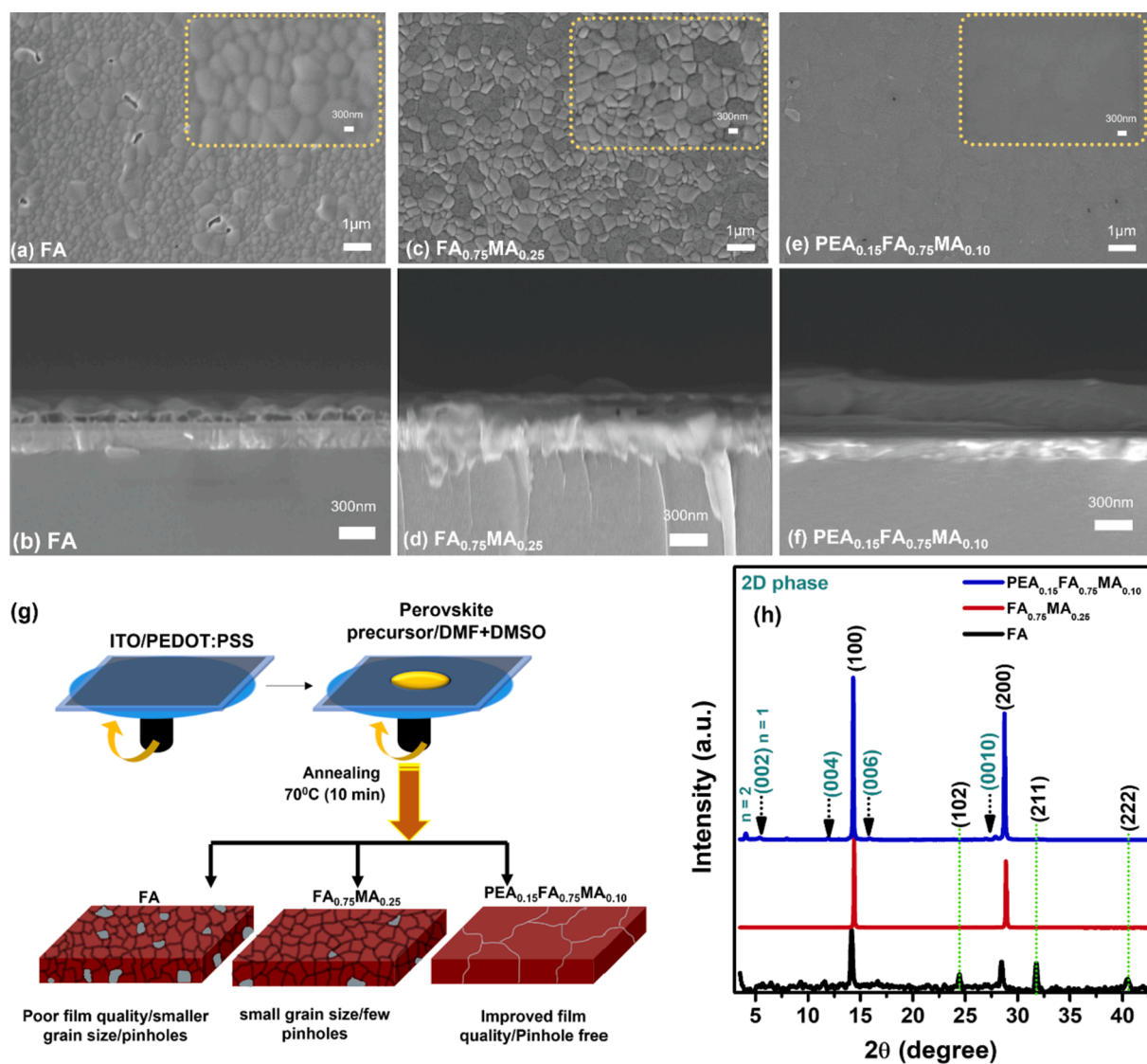


**Fig. 1.** (a-f) Field emission scanning electron microscopy (FE-SEM) micrographs for FA,  $\text{FA}_{0.75}\text{MA}_{0.25}$  and  $\text{PEA}_{0.15}\text{FA}_{0.75}\text{MA}_{0.10}$  at a scale of 1  $\mu\text{m}$  and 300 nm (inset images), (g) Schematic representation of perovskite film fabrication, compositional engineering through  $\text{PEA}^+$  cation substitution at A site and how it helps in improving the film uniformity. (h) Comparative X-ray diffraction (XRD) patterns of FA,  $\text{FA}_{0.75}\text{MA}_{0.25}$  and  $\text{PEA}_{0.15}\text{FA}_{0.75}\text{MA}_{0.10}$  perovskites.



has been observed that, the substitution of  $\text{PEA}^+$  cation in 3D perovskite forms 2D phase as well [39,43], so it can be expected that the  $\text{PEA}_{0.15}\text{FA}_{0.75}\text{MA}_{0.10}$  exhibits both 2D/3D perovskite phase [44,45]. Furthermore, the FE-SEM micrograph (Fig. 1(e-f)) depicts the formation of smoother and highly compact film. The grain boundaries are not clearly visible in  $\text{PEA}_{0.15}\text{FA}_{0.75}\text{MA}_{0.10}$ , which may be attributed to existence of 2D phase (flakes) which helps to fuse 3D perovskite phase and hence lessen the visibility of grain boundaries.

Fig. S1 depicts the FE-SEM micrographs for  $x = 0.05, 0.10$  and  $0.20$  added  $\text{PEA}_x\text{FA}_{0.75}\text{MA}_{0.25-x}\text{SnI}_2\text{Br}$  as well. At the initial concentration, the FE-SEM micrograph depicts smooth morphology with several pinholes, which further reduced with  $x = 0.10$  PEA substituted perovskite. The optimized concentration of  $\text{PEA}^+$  in  $\text{PEA}_x\text{FA}_{0.75}\text{MA}_{0.25-x}\text{SnI}_2\text{Br}$  is  $x = 0.15$  (Fig. 1(e)), beyond this point since the concentration of  $\text{PEA}^+$  is more, it resulted the formation of more flakes like morphology (Fig. S1(c)) led to excessive 2D perovskite phase, in addition there are certain pinhole that can be seen from the inset graph in Fig. S1(c). The schematic for perovskite film fabrication is shown in Fig. 1(g), where all the three conditions are depicted pictorially. The initial FA and  $\text{FA}_{0.75}\text{MA}_{0.25}$  resulted in worst film quality, however in comparison  $\text{PEA}_{0.15}\text{FA}_{0.75}\text{MA}_{0.10}$  resulted in smooth and uniform perovskite film through compositional modification, the above results revealed that the addition of hydrophobic organic cation in an optimized ratio helps in supporting better film quality with uniformity, and no pinholes. In other words, hydrophobic  $\text{PEA}^+$  cations passivate the grain boundary of 3D perovskite to form a 2D/3D perovskite film, thereby reducing pinholes, improve uniformity and smoothness to form a better-quality perovskite film.

To further investigate on crystal growth, XRD measurement was conducted as shown in Fig. 1(h). Black and red line depicts XRD pattern of FA with crystalline peaks at  $14.1^\circ$ ,  $24.4^\circ$ ,  $28.4^\circ$ ,  $31.8^\circ$  and  $40.47^\circ$  corresponds to (100), (102), (200), (211) and (222) ( $hkl$ ) planes of 3D perovskite, as reported elsewhere in literature [31]. The substitution of  $\text{FA}^+$  cation with  $\text{MA}^+$  cation in  $\text{FA}_{0.75}\text{MA}_{0.25}$  perovskite clearly depicts the existence of two major ( $hkl$ ) planes at (100) and (200) corresponds to the 3D perovskite phase and no other impurity peaks were observed. In case of  $\text{PEA}_{0.15}\text{FA}_{0.75}\text{MA}_{0.10}$  (blue line), apart from 3D phase the existence of quasi 2D perovskite phase can be clearly observed at lower lattice reflections at  $4.12^\circ$ ,  $5.4^\circ$  and  $8.0^\circ$ , attributed to 2D perovskite for  $n = 1$  and  $n = 2$  compositions [46–48], additionally the lattice reflections at  $11.8^\circ$ ,  $15.7^\circ$  and  $27.0^\circ$  corresponds to (004), (006) and (0010) ( $hkl$ ) planes for quasi-2D perovskite [49,50], which indicates the existence of 2D/3D mixed perovskite in  $\text{PEA}_{0.15}\text{FA}_{0.75}\text{MA}_{0.10}$ . Notably, the diffraction pattern for  $\text{FA}_{0.75}\text{MA}_{0.25}$  shows a slight shift towards higher angle, most likely caused by the substitution of large  $\text{FA}^+$  cation with the smaller one [51,52]. However, the consistency in XRD peak positionings was observed with the substitution of  $\text{PEA}^+$  cation in  $\text{FA}_{0.75}\text{MA}_{0.25}$  perovskite (Fig. 1(h) blue line). Due to comparatively large size of  $\text{PEA}^+$  cation [53] the substitution resulted in the formation of quasi 2D phase along with 3D perovskite as can be seen from the XRD

pattern for  $\text{PEA}_{0.15}\text{FA}_{0.75}\text{MA}_{0.10}$ . Substituting  $\text{PEA}^+$  cation in 3D perovskite resulted in the formation of 2D/3D mixed perovskite and these 2D perovskite entities help to merge 3D perovskite grains together and reduce the grain boundaries.

Grazing-incidence wide-angle X-ray scattering (GIWAXS) measurement was performed to investigate the crystal orientation in 2D/3D perovskite ( $\text{PEA}_{0.15}\text{FA}_{0.75}\text{MA}_{0.10}$ ) in comparison with the 3D perovskite film ( $\text{FASnI}_2\text{Br}$ ), instrumental detail is provided in the SI. Fig. 2, depicts the 2D scattering spectra of both the samples consisting of ITO/PEDOT: PSS/perovskite at an incident angle of  $0.12^\circ$ . The Debye-Scherrer rings in Fig. 2(a) corresponds to 3D perovskite ( $\text{FASnI}_2\text{Br}$ ) with polycrystalline reflections that matches well with the XRD data as presented in Fig. 1(h). On the other hand, 2D/3D perovskite ( $\text{PEA}_{0.15}\text{FA}_{0.75}\text{MA}_{0.10}$ ) scattering spectrum depicts intense Bragg spots as shown in Fig. 2(b), where Bragg spots located along the  $q_z$  direction at (100) and (200) at  $q_z \sim -2.0 \text{ \AA}^{-1}$  and  $q_z \sim -0.5 \text{ \AA}^{-1}$ , which corresponds to the preferred orientation of 3D perovskite in  $\text{PEA}_{0.15}\text{FA}_{0.75}\text{MA}_{0.10}$  perovskite. The preferred growth in  $\text{PEA}_{0.15}\text{FA}_{0.75}\text{MA}_{0.10}$  perovskite as analyzed through GIWAXS corroborates well with the XRD study as discussed above. This has been further confirmed with the line cut profile GIWAXS data as provided in the SI as Fig. S2, where the preferential growth of  $h00$  reflection planes can be noticed in  $\text{PEA}_{0.15}\text{FA}_{0.75}\text{MA}_{0.10}$  as compared to  $\text{FASnI}_2\text{Br}$ , confirms the preferential growth in 2D/3D mixed perovskite. Notably Fig. 2(b) shows Bragg spot just below (100) plane in  $\text{PEA}_{0.15}\text{FA}_{0.75}\text{MA}_{0.10}$  corresponds to 2D perovskite phase [54], which is not detected in the scattering spectra of  $\text{FASnI}_2\text{Br}$ . GIWAXS and line cut profile analysis for 2D/3D mixed perovskites mentioned in the previous studies suggest that reflection peak positioned at (002) corresponds to the single layer ( $n = 1$ ) of 2D perovskite [45]. However, it is speculated that  $\text{PEA}_{0.15}\text{FA}_{0.75}\text{MA}_{0.10}$  is a quasi 2D/3D mixed perovskite, since the quasi 2D perovskites not only comprises of single phase, but it contains multiple  $n$  phases, as reported in the previous studies [47] and observed through XRD analysis in the present investigation as well.

The absorption spectrum for FA is shown in Fig. 3(a) in the wavelength range of 300 nm to 900 nm, with the estimated bandgap ( $E_g$ ) of 1.68 eV (Fig. S3), calculated using Tauc plot, closely matched with the  $E_g$  for  $\text{FASnI}_2\text{Br}$  as reported elsewhere [32]. In comparison to FA,  $\text{FA}_{0.75}\text{MA}_{0.25}$  and  $\text{PEA}_{0.15}\text{FA}_{0.75}\text{MA}_{0.10}$  absorption spectra are also depicted (red and blue graphs, Fig. 3(a)). The light absorption intensity slightly increases in  $\text{FA}_{0.75}\text{MA}_{0.25}$  perovskite, with a red shift in absorption edge with the estimated bandgap of 1.62 eV (Fig. S3), which is almost like the reported literature [28]. Furthermore, we measured the absorption spectra for  $\text{PEA}_x\text{FA}_{0.75}\text{MA}_{0.25-x}\text{SnI}_2\text{Br}$  films ( $x = 0.05, 0.10, 0.15$  and  $0.20$ ) shown in Fig. S3(a), a slight blue shift has been noticed with the increasing ratios of PEA. Blue shift in absorption edge for  $\text{PEA}_{0.15}\text{FA}_{0.75}\text{MA}_{0.10}$  can be observed in comparison to  $\text{FA}_{0.75}\text{MA}_{0.25}$  perovskite with an estimated bandgap in the range from 1.63 to 1.66 eV with increasing  $\text{PEA}^+$  cation ratio (depicted in Fig. S3(b)). Compared to FA perovskite the increase in the absorbance signal for  $\text{FA}_{0.75}\text{MA}_{0.25}$  is quite visible, which relates to the improved crystallinity and large grain

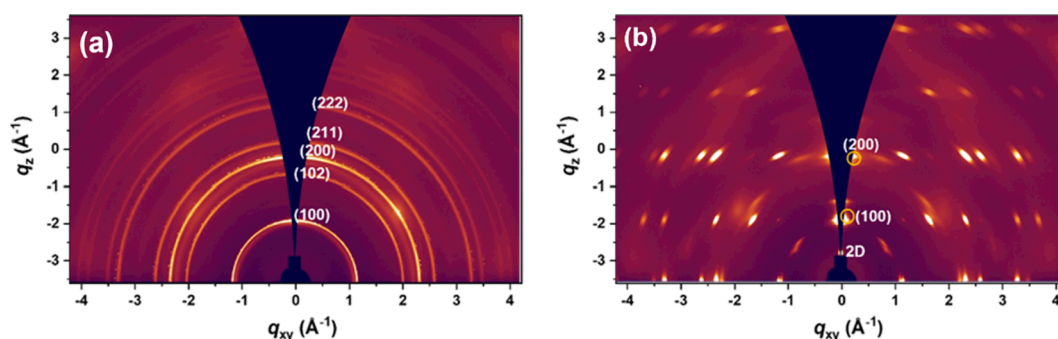
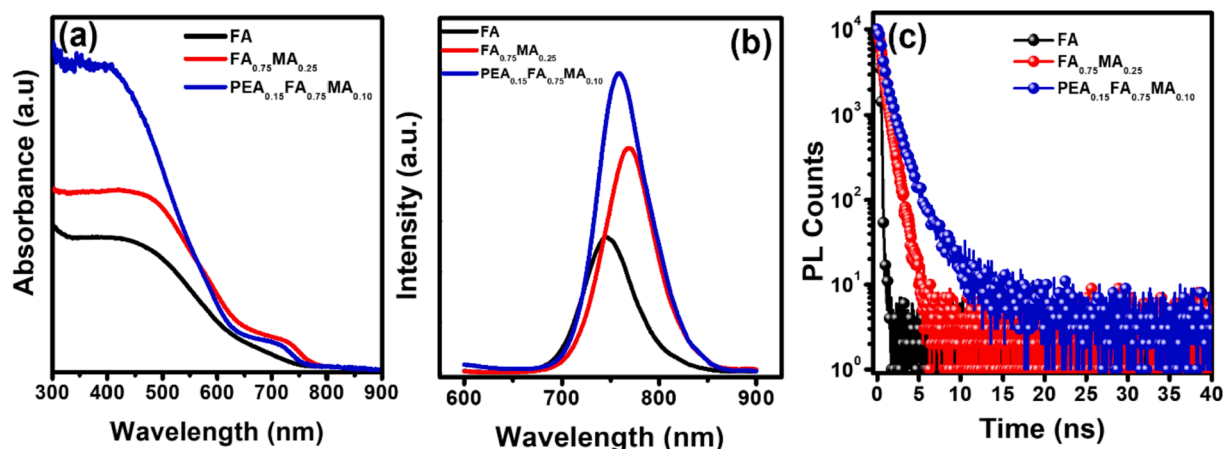


Fig. 2. Grazing-incidence wide-angle X-ray scattering (GIWAXS) images of (a)  $\text{FASnI}_2\text{Br}$  and (b)  $\text{PEA}_{0.15}\text{FA}_{0.75}\text{MA}_{0.10}\text{SnI}_2\text{Br}$ . GIWAXS patterns were obtained at an incident angle of  $0.12^\circ$ .



**Fig. 3.** Comparative (a) UV-vis absorption, (b) steady-state PL and (c) time-resolved PL spectra for FA (Black line), FA<sub>0.75</sub>MA<sub>0.25</sub> (Red line) and PEA<sub>0.15</sub>FA<sub>0.75</sub>MA<sub>0.10</sub> (Blue line).

size [55]. The perovskite crystallinity improved in FA<sub>0.75</sub>MA<sub>0.25</sub> due to an effect of MA substitution [51]. While in FA and FA<sub>0.75</sub>MA<sub>0.25</sub> perovskite the absorbance signals purely indicate the existence of 3D phase, in PEA<sub>x</sub>FA<sub>0.75</sub>MA<sub>0.25-x</sub>SnI<sub>2</sub>Br perovskites we have observed the presence of additional signal in the range of 400 to 430 nm range, attributes to the formation of 2D/3D perovskite and the intensity variation seemed to be executed by the ratio of PEA<sup>+</sup> cation substitution (Fig. S3 (a)). However, the absorption signal shows a dip with further increasing ratio of PEA<sup>+</sup> cation ( $x = 0.20$ ). As depicted from the FE-SEM micrograph of PEA<sub>0.20</sub>FA<sub>0.75</sub>MA<sub>0.05</sub>, higher concentration of PEA<sup>+</sup> cation led to the formation of excess 2D phase that may affect the absorption signals from 3D perovskite probably due to loss of 3D perovskite structure [39,56–58], which is quite evident from the absorption spectrum of PEA<sub>0.20</sub>FA<sub>0.75</sub>MA<sub>0.05</sub> perovskite from Fig. S3(a). Fig. 3(b) shows the steady state PL (SS-PL) spectra for FA, FA<sub>0.75</sub>MA<sub>0.25</sub> and PEA<sub>0.15</sub>FA<sub>0.75</sub>MA<sub>0.10</sub> films coated on glass substrate and measurement was conducted from the front side with all the parameters kept constant throughout the measurement. The PL peak position 745 nm has been observed for FA case, which is in accordance with the PL wavelength as reported in the literature [32], soon with the addition of MA<sup>+</sup> cation in mixed cation perovskite (namely FA<sub>0.75</sub>MA<sub>0.25</sub>, red line in Fig. 3(b)) we observed a red shift of 22 nm in the PL wavelength with the peak position at around 767 nm, consistent with the shift in absorption spectrum. With the incorporation of PEA<sup>+</sup> cation in mixed cation perovskite i.e., PEA<sub>0.15</sub>FA<sub>0.75</sub>MA<sub>0.10</sub> (Blue line Fig. 3(b)), PL position further shifted towards lower wavelength at 758 nm, attributes to increased quantum confinement, which relates to the existence of 2D layered perovskite structure. The blue shift in absorption edge and PL spectrum for PEA<sub>0.15</sub>FA<sub>0.75</sub>MA<sub>0.10</sub> with respect to FA<sub>0.75</sub>MA<sub>0.25</sub> might be attributed to the formation of 2D layered perovskite phase along with 3D perovskite [43,59], as evident from the FE-SEM results in prior discussion. Reports suggest that improved crystallographic interaction between 2D/3D perovskite suppress the charge carrier recombination, resulted in enhancement in PL intensity. We may assume that better electronic interfacing between 2D/3D perovskite phase and improved crystallinity of perovskite (PEA<sub>0.15</sub>FA<sub>0.75</sub>MA<sub>0.10</sub>), which further relates to reduced trap densities and increase in PL intensity [60–63].

We have further conducted time-resolved PL (TRPL) measurement (shown in Fig. 3(c)) for FA, FA<sub>0.75</sub>MA<sub>0.25</sub> and PEA<sub>0.15</sub>FA<sub>0.75</sub>MA<sub>0.10</sub> perovskite films on glass substrate to verify the results as observed through SS-PL and the average lifetime calculated using the equation (1) from supporting information (SI) [64]. Fitting was done biexponentially and the related parameters are listed in Table S1 (SI). The average carrier lifetimes ( $\tau_{avg}$ ) of all the cases determined as 0.10 ns (FA), 0.65 ns (FA<sub>0.75</sub>MA<sub>0.25</sub>) and 1.25 ns (PEA<sub>0.15</sub>FA<sub>0.75</sub>MA<sub>0.10</sub>), respectively. The increased carrier lifetime as observed from TRPL and PL intensity

enhancement in SS-PL attributes to lower defect density and grain boundaries passivation in 2D/3D perovskite relates to perovskite film with improved crystallinity [56,65]. These results suggest that adding optimal ratio of organic cation in 3D mixed halide perovskites helps to develop uniform perovskite film, which is beneficial to attain improved device performance in WBG Sn PSCs.

XPS measurement was carried out to detect the chemical states of Sn (Tin), Br (Bromine) and N (Nitrogen) in FA, FA<sub>0.75</sub>MA<sub>0.25</sub> and PEA<sup>+</sup> substituted perovskites i.e., PEA<sub>0.15</sub>FA<sub>0.75</sub>MA<sub>0.10</sub>, the survey scan for all three perovskites is provided in supporting information (SI) as Fig. S4. It has been observed that the binding energy (BE) peak intensity of oxygen is reduced for PEA<sub>0.15</sub>FA<sub>0.75</sub>MA<sub>0.10</sub> as compared to other two cases which further confirm that addition of hydrophobic PEA<sup>+</sup> cation reduce the penetration of moisture/oxygen and may help to enhance perovskite stability. Fig. 4 (a–c) depicts the XPS core spectra for Sn 3d, Br 3d and N 1s respectively, rectified with C 1s calibrated at 284.6 eV ~BE [66]. Furthermore, XPS core spectra of Sn 3d was studied to understand the inhibition of Sn<sup>2+</sup> oxidation with the substitution of PEA<sup>+</sup> organic cation in 3D perovskite. Two broad peaks in Sn 3d core spectra were detected which relates to Sn 3d<sub>5/2</sub> and Sn 3d<sub>3/2</sub>, with an energy separation of 8.4 eV [67]. For the case of FA and FA<sub>0.75</sub>MA<sub>0.25</sub> the BEs of Sn 3d at 486.6 eV (495.1 eV) and 486.4 eV (494.7 eV) corresponds to Sn 3d<sub>5/2</sub> (Sn 3d<sub>3/2</sub>) contributions [36,40], as shown in Fig. 4(a). However, a shift of 0.6 eV towards lower BEs is observed for PEA<sub>0.15</sub>FA<sub>0.75</sub>MA<sub>0.10</sub> i.e., 486.0 eV (Sn 3d<sub>5/2</sub>) and 494.4 eV (Sn 3d<sub>3/2</sub>) with respect to FASnI<sub>2</sub>Br BEs, where the BE at 486.0 eV and 494.4 eV in PEA<sub>0.15</sub>FA<sub>0.75</sub>MA<sub>0.10</sub> corresponds to the Sn<sup>2+</sup> oxidation state, similar to the reported literature [68]. As previous studies suggest that the shift in BE peaks in XPS relates to the change in oxidation states of the element, i.e., higher BEs corresponds to the higher oxidation state known as chemical shift [69,70]. The calculated percentages of Sn<sup>2+</sup> and Sn<sup>4+</sup> are provided in Table S2 obtained from the deconvolution of XPS spectra. It has been observed that Sn<sup>4+</sup> percentage decreased from 64.2% for FA to 16.9% for PEA<sub>0.15</sub>FA<sub>0.75</sub>MA<sub>0.10</sub>. The ease oxidation of Sn perovskites relates to the penetration of moisture which is the major source of perovskite degradation. Presence of hydrophobic organic cations with aromatic rings helps in suppressing moisture penetration and enhance the stability in perovskites [36,71]. Hence, we could expect that the substitution of PEA<sup>+</sup> in 3D WBG Sn perovskite (PEA<sub>0.15</sub>FA<sub>0.75</sub>MA<sub>0.10</sub>) helps in reducing moisture/oxygen penetration and further oxidation to Sn<sup>4+</sup> state [40]. In addition, the BE signals for Br 3d at 67.9 eV and 68.9 eV in FA and FA<sub>0.75</sub>MA<sub>0.25</sub> corresponds to Br 3d<sub>5/2</sub> and Br 3d<sub>3/2</sub> states, as depicted in Fig. 4(b) [72]. However, the deconvoluted spectrum of PEA<sub>0.15</sub>FA<sub>0.75</sub>MA<sub>0.10</sub> depicted slight shift towards higher BEs, might be attributed to hydrogen or ionic interactions between halide ions and NH<sup>3+</sup> groups of organic cations [66,73]. To further evident the existence of PEA<sup>+</sup> cation in WBG Sn

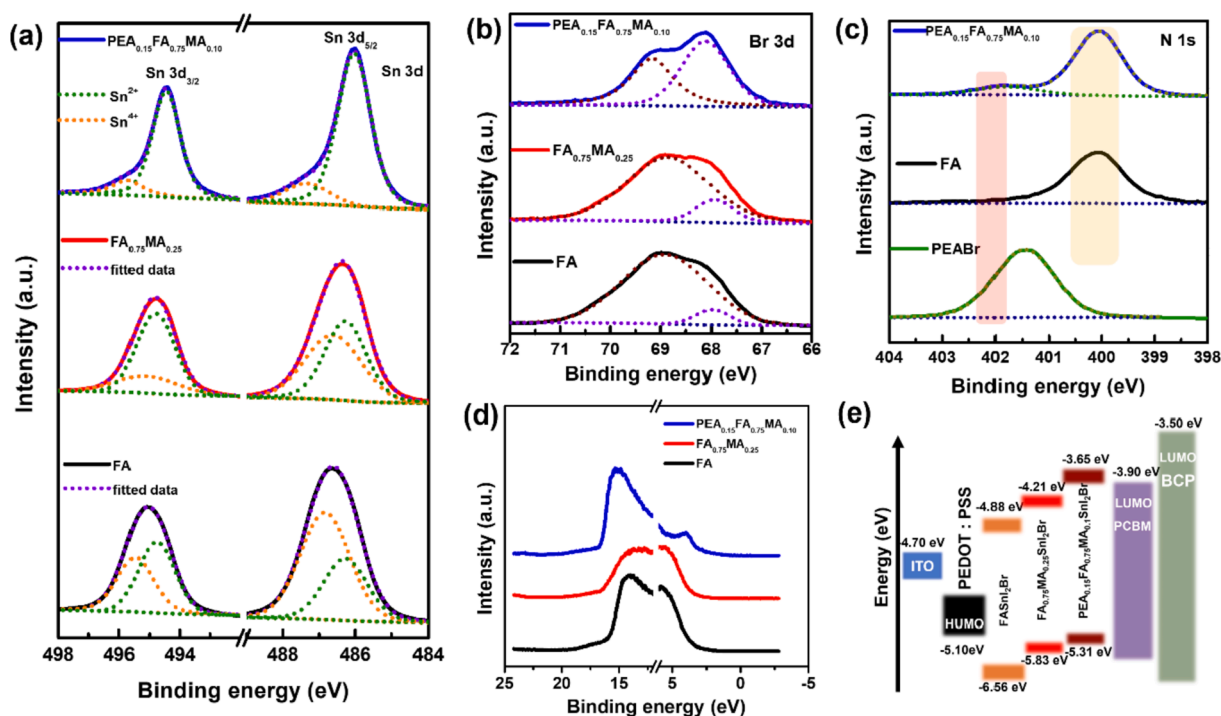


**Fig. 4.** (a-b) Comparative Sn 3d and Br 3d XPS core spectra for FA,  $\text{FA}_{0.75}\text{MA}_{0.25}$ , and  $\text{PEA}_{0.15}\text{FA}_{0.75}\text{MA}_{0.10}$  (c) N 1s core spectra for FA and  $\text{PEA}_{0.15}\text{FA}_{0.75}\text{MA}_{0.10}$  in comparison with N 1s core spectra of PEABr (Green line). (d-e) UPS spectra and energy band alignment for FA,  $\text{FA}_{0.75}\text{MA}_{0.25}$  and  $\text{PEA}_{0.15}\text{FA}_{0.75}\text{MA}_{0.10}$  with respect to ETL/HTL in complete p-i-n device architecture.

perovskite N 1s core spectra for PEABr, FA and  $\text{PEA}_{0.15}\text{FA}_{0.75}\text{MA}_{0.10}$  were analyzed as shown in Fig. 4(c). The N 1s peak for PEABr located at 401.5 eV and for FASnBr (FA) the peak located at 400.1 eV ascribed to the signature peak of  $\text{C}=\text{NH}_2^+$  from  $\text{FA}^+$  cation [40,74]. On the other hand, the deconvoluted N 1s core spectrum of  $\text{PEA}_{0.15}\text{FA}_{0.75}\text{MA}_{0.10}$  (Blue spectrum Fig. 4(c)) depicted two peaks located at 401.8 eV related to N 1s peak from PEABr and at 400.1 eV which resembles to N 1s peak from FA, hence evident the presence of  $\text{PEA}^+$  cation in WBG Sn perovskite.

We have further conducted ultraviolet photoelectron spectroscopy (UPS) measurement on FA,  $\text{FA}_{0.75}\text{MA}_{0.25}$  and  $\text{PEA}_{0.15}\text{FA}_{0.75}\text{MA}_{0.10}$  perovskites as shown in Fig. 4(d), to elucidate the energy band alignments as an effect of  $\text{MA}^+$  and  $\text{PEA}^+$  cation substitution in WBG Sn perovskite. The left panel in Fig. 4(d) shows the high binding energy (HBE) cut off, through which work function ' $\phi$ ' of perovskite calculated to be  $-4.82$  eV,  $-4.29$  eV and  $-4.36$  eV for FA,  $\text{FA}_{0.75}\text{MA}_{0.25}$  and  $\text{PEA}_{0.15}\text{FA}_{0.75}\text{MA}_{0.10}$  respectively, using the equation (2) from SI [75]. Furthermore, the valance band maxima (VBM) were obtained by subtracting  $\phi$  with the corresponding valance band (VB) edge value as depicted in the right panel of Fig. 4(d). The VBM values of  $-6.56$  eV,  $-5.83$  eV (consistent with the reported literature) [28] and  $-5.31$  eV were calculated for FA,  $\text{FA}_{0.75}\text{MA}_{0.25}$  and  $\text{PEA}_{0.15}\text{FA}_{0.75}\text{MA}_{0.10}$ , respectively. The conduction band minima (CBM) were obtained by scaling VBM energies with the related bandgaps (calculated using Tauc plots, as shown in Fig. S3(b)), hence the corresponding values are  $-4.88$  eV,  $-4.21$  eV and  $-3.65$  eV for FA,  $\text{FA}_{0.75}\text{MA}_{0.25}$  and  $\text{PEA}_{0.15}\text{FA}_{0.75}\text{MA}_{0.10}$  respectively. The band alignment of FA,  $\text{FA}_{0.75}\text{MA}_{0.25}$  and  $\text{PEA}_{0.15}\text{FA}_{0.75}\text{MA}_{0.10}$  with respect to HTL/ETL in a device assembly are depicted in Fig. 4(e), as estimated from the approximate values. The mechanism of bandgap modification in Sn based perovskites is quite different than Pb based halide perovskites. Sn s and halogen (I/Br) p antibonding orbitals contributes to the formation of VB and Sn p and I/Br p orbitals of more nonbonding participates in CB formation, hence develop the band structure in Sn perovskites. Whereas A site cation counterbalance the whole perovskite structure and have an impact on the overlapping of metal-halide

molecular orbitals. In Sn perovskites the substitution of large cation with the smaller size cation leads to bandgap reduction as can be seen from the above results, where the partial substitution of  $\text{FA}^+$  (2.79 Å) with  $\text{MA}^+$  (2.70 Å) [76] tends to modulate the bandgap from 1.68 eV to 1.62 eV, so do the relative red shift in PL spectrum was observed. We further find the correlation between the bandgap modifications with the UPS study, as observed the VBM upshifted for  $\text{FA}_{0.75}\text{MA}_{0.25}$  in comparison to FA perovskite. Since the substitution with smaller size  $\text{A}^+$  site cation in Sn perovskite results in lattice contraction [77], which indicates shortening of metal-halide bond and hence increased overlapping of orbitals. The raise in VBM for  $\text{FA}_{0.75}\text{MA}_{0.25}$  corresponds to the modifications in perovskite lattice which tends to reduction in metal-halide bond. In other words, the overlapping between metal-halide increases which affect the antibonding orbital states corresponds to shift in VBM to higher energy and reduction in bandgap. Furthermore, with the substitution of  $\text{PEA}^+$  organic cation in 3D mixed cation WBG Sn perovskite (namely  $\text{PEA}_{0.15}\text{FA}_{0.75}\text{MA}_{0.10}$ ) that leads to the formation of 2D/3D perovskite, the band energy diagram depicts upshift of CBM energy, which enables efficient electron injection from perovskite to ETL. In FA perovskite the VBM energy is approx.  $-6.56$  eV attributes to oxidation of Sn as reported elsewhere [51]. Hence it is considered that lowering of VBM in Sn perovskites relates to the conversion of  $\text{Sn}^{2+}$  to  $\text{Sn}^{4+}$ . However, the VBM energy values upshifted for  $\text{FA}_{0.75}\text{MA}_{0.25}$  ( $-5.83$  eV) and further upshifting was observed for  $\text{PEA}^+$  perovskite to  $-5.31$  eV, ascribe to reduced rate of oxidation in 2D/3D perovskite as corroborated with the XPS results. It can be supposed that substitution at A site cation with appropriate and optimal ratio of hydrophobic organic cation helps in modulating the band energy levels for better alignment with ETL/HTL in device assembly in order to allow for efficient electron injection processes [78].

Since our results suggest that optimal  $\text{PEA}^+$  organic cation here reduce the level of phase degradation by controlling the rate of  $\text{Sn}^{2+}$  to  $\text{Sn}^{4+}$  oxidation. To further testify this phenomenon, we have opt the stability test through absorbance measurement on FA,  $\text{FA}_{0.75}\text{MA}_{0.25}$  and  $\text{PEA}_{0.15}\text{FA}_{0.75}\text{MA}_{0.10}$  perovskite films on glass substrates. Fig. 5(a)



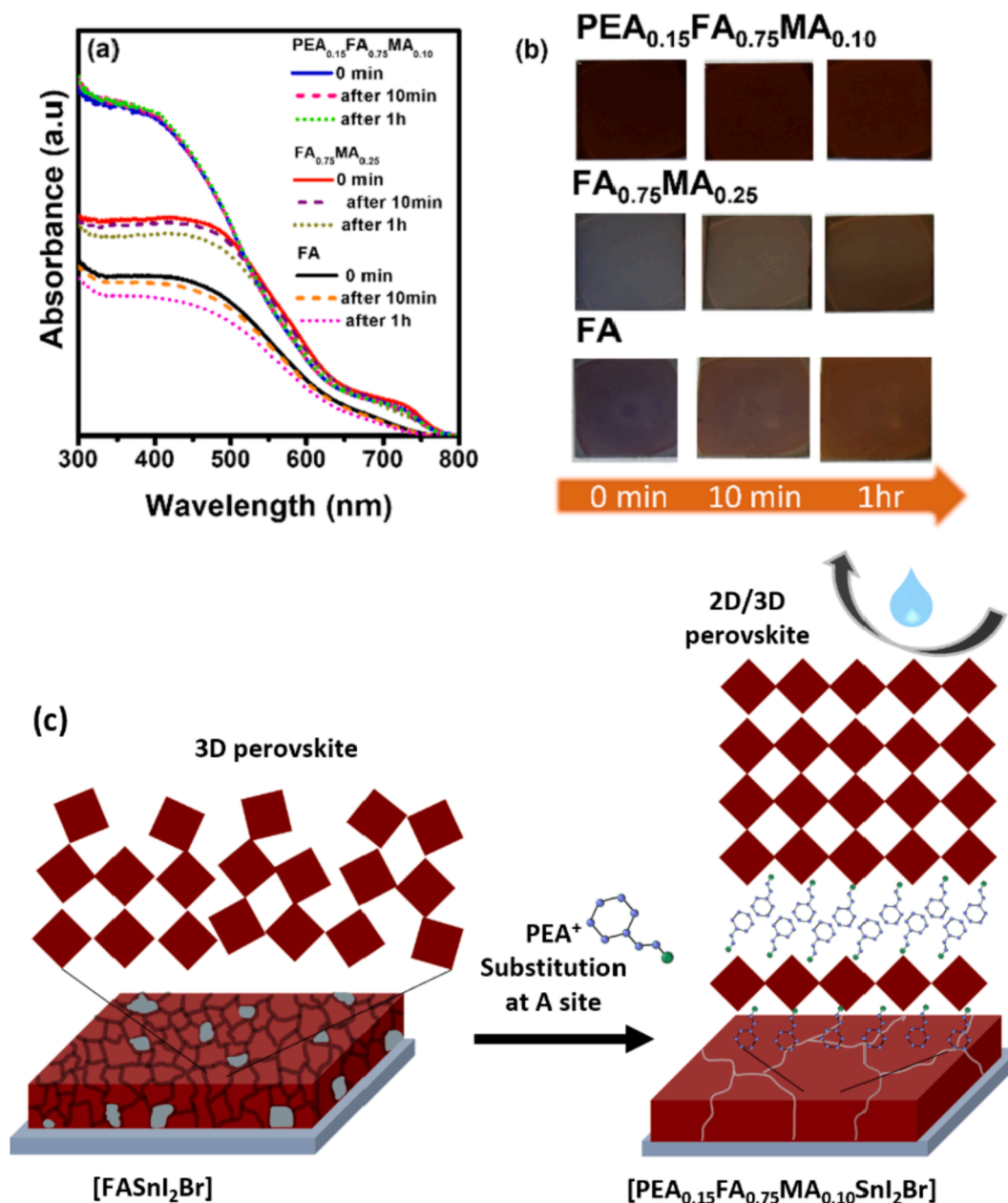


**Fig. 5.** (a-b) Absorption spectra and images for FA,  $\text{FA}_{0.75}\text{MA}_{0.25}$  and  $\text{PEA}_{0.15}\text{FA}_{0.75}\text{MA}_{0.10}$  at different interval of time with exposure and related degradation. (c) Schematic illustration on how  $\text{PEA}^+$  cation substitution at A site in a mixed cation 3D perovskite helps in reducing moisture penetration brings ambient stability, improve film uniformity, and passivate defects.

depicts the absorbance spectra for FA,  $\text{FA}_{0.75}\text{MA}_{0.25}$  and  $\text{PEA}_{0.15}\text{FA}_{0.75}\text{MA}_{0.10}$  at 0 min, after 10 min and after 1 h exposure in ambient atmospheric conditions. Fig. 5(b) displayed the images of FA,  $\text{FA}_{0.75}\text{MA}_{0.25}$  and  $\text{PEA}_{0.15}\text{FA}_{0.75}\text{MA}_{0.10}$  after certain time intervals, which revealed clear degradation of FA and  $\text{FA}_{0.75}\text{MA}_{0.25}$  perovskites, however we have not observed such degradation for  $\text{PEA}_{0.15}\text{FA}_{0.75}\text{MA}_{0.10}$  perovskite. The absorption spectra for FA and  $\text{FA}_{0.75}\text{MA}_{0.25}$  perovskite (Fig. 5(a)) shows slight decrease in the absorption after 10 mins exposure and further loss was very much visible after 1 h exposure which suggest the degradation of Sn perovskite due to moisture/oxygen penetration. On the other hand, for  $\text{PEA}_{0.15}\text{FA}_{0.75}\text{MA}_{0.10}$  perovskite no such degradation was observed, which suggest that hydrophobic  $\text{PEA}^+$  cation in 2D/3D perovskite helps in protecting the 3D structure and restrict the penetration of moisture/oxygen through grain boundaries. Based on all the above evidence, the plausible schematics can be depicted as shown in Fig. 5(c). The

schematic illustration indicates that the substitution of appropriate ratio of  $\text{PEA}^+$  cation in 3D perovskite precursor benefits in several ways. Previous study suggests that diffraction peaks at  $5.5^\circ$ – $4.0^\circ$  corresponds to  $n = 1$  and 2 structures of 2D perovskite layers that forms at early stage of annealing, however the 3D structure growth keep increasing with further annealing. Notably, low dimensional perovskite phase further execute the growth of 3D perovskite and act as template [41]. Based on GIWAXS analysis we may speculate that 2D perovskite corresponds to  $n = 1$  and 2 layers exist in the proximity of the substrate in perovskite film as well [39], suggesting that formation of 2D perovskite structure at an early stage of annealing further guide the preferential growth of 3D perovskite during the annealing process. It also helps in merging 3D perovskite grain boundaries which is one of the major causes for moisture penetration in perovskite films leads to degradation. The random orientation, formation of poor-quality perovskite film and moisture penetration can be illustrated for 3D WBG Sn perovskite, however the

substitution of A site cation with hydrophobic PEA<sup>+</sup> cation in 2D/3D perovskite mitigate these issues. Furthermore, as considering one of the major issues in WBG Sn perovskites is poor band alignment with CTLs and  $V_{oc}$  deficit, above observations and analysis through UPS study suggest that 2D/3D perovskite exhibit better band alignment for efficient charge transfer.

To elucidate the role of PEA<sup>+</sup> cation substitution in 3D WBG Sn perovskite we further explored device performance by employing FA, FA<sub>0.75</sub>MA<sub>0.25</sub> and PEA<sub>x</sub>FA<sub>0.75</sub>MA<sub>0.25-x</sub>SnI<sub>2</sub>Br perovskites as WBG photoabsorbers in p-i-n device architecture with device structure of glass/ITO/PEDOT:PSS/WBG Sn Perovskite/PCBM/BCP/Ag. Fig. 6(a) and Fig. S5 represented the current density ( $J_{sc}$ ) vs voltage ( $V_{oc}$ ) (J-V) characteristics for FA, FA<sub>0.75</sub>MA<sub>0.25</sub> and PEA<sub>x</sub>FA<sub>0.75</sub>MA<sub>0.25-x</sub>SnI<sub>2</sub>Br (x = 0.05, 0.10, 0.15, 0.20) based PSCs. FA based device acquires poor performance of 2.38% with  $J_{sc}$  of 8.29  $\text{mA}\cdot\text{cm}^{-2}$  and  $V_{oc}$  of 0.46 V (Fig. 6(a) black line), which showed slight increase in device performance for FA<sub>0.75</sub>MA<sub>0.25</sub> to 3.66% with  $J_{sc}$  of 10.95  $\text{mA}\cdot\text{cm}^{-2}$  and  $V_{oc}$  of 0.48 V, relates to the above findings. Moving to the PEA<sup>+</sup> cation substituted WBG Sn perovskite, with initial substitution in PEA<sub>0.05</sub>FA<sub>0.75</sub>MA<sub>0.20</sub> all the device parameters increased (Fig. S5), and the device acquires PCE

of 6.33%, which slightly increased to 6.56% for PEA<sub>0.10</sub>FA<sub>0.75</sub>MA<sub>0.15</sub> with enhanced  $V_{oc}$  of 0.64 V and  $J_{sc}$  of 14.36  $\text{mA}\cdot\text{cm}^{-2}$ . A significant enhancement in device efficiency for PEA<sub>0.15</sub>FA<sub>0.75</sub>MA<sub>0.10</sub> has been achieved with respectably high PCE of 7.96% for the champion device with the  $J_{sc}$  of 16.89  $\text{mA}\cdot\text{cm}^{-2}$ ,  $V_{oc}$  of 0.67 V and FF of 70.36% (Shown in Fig. 6(a) Blue line) and certified PCE of 7.84% (shown in the SI as Fig. S6). To check with the reproducibility aspect, we have tested 27 set of devices for FA, FA<sub>0.75</sub>MA<sub>0.25</sub> and PEA<sub>0.15</sub>FA<sub>0.75</sub>MA<sub>0.10</sub> each case, and 12 set of devices for PEA<sub>0.05</sub>FA<sub>0.75</sub>MA<sub>0.20</sub>, PEA<sub>0.10</sub>FA<sub>0.75</sub>MA<sub>0.15</sub> and PEA<sub>0.20</sub>FA<sub>0.75</sub>MA<sub>0.05</sub>, respectively. Fig. S7 represents the statistical distribution of device parameters and the best device efficiencies are tabulated in Table S3 (SI). Our observations revealed that minimal substitution of PEA<sup>+</sup> cation in WBG Sn perovskite (PEA<sub>0.05</sub>FA<sub>0.75</sub>MA<sub>0.20</sub> and PEA<sub>0.10</sub>FA<sub>0.75</sub>MA<sub>0.15</sub>) suffers from several pinholes which ultimately affect the device performance as can be seen from the results. Gradually increasing PEA<sup>+</sup> ratio up to PEA<sub>0.15</sub>FA<sub>0.75</sub>MA<sub>0.10</sub> led to the formation of uniform, preferentially oriented film with reduced defects which seems useful to device efficiency enhancement. Furthermore, the device efficiency reduced (Fig. S5) for PEA<sub>0.20</sub>FA<sub>0.75</sub>MA<sub>0.05</sub>, might be attributed to the existence of excess 2D perovskite as compared to the 3D

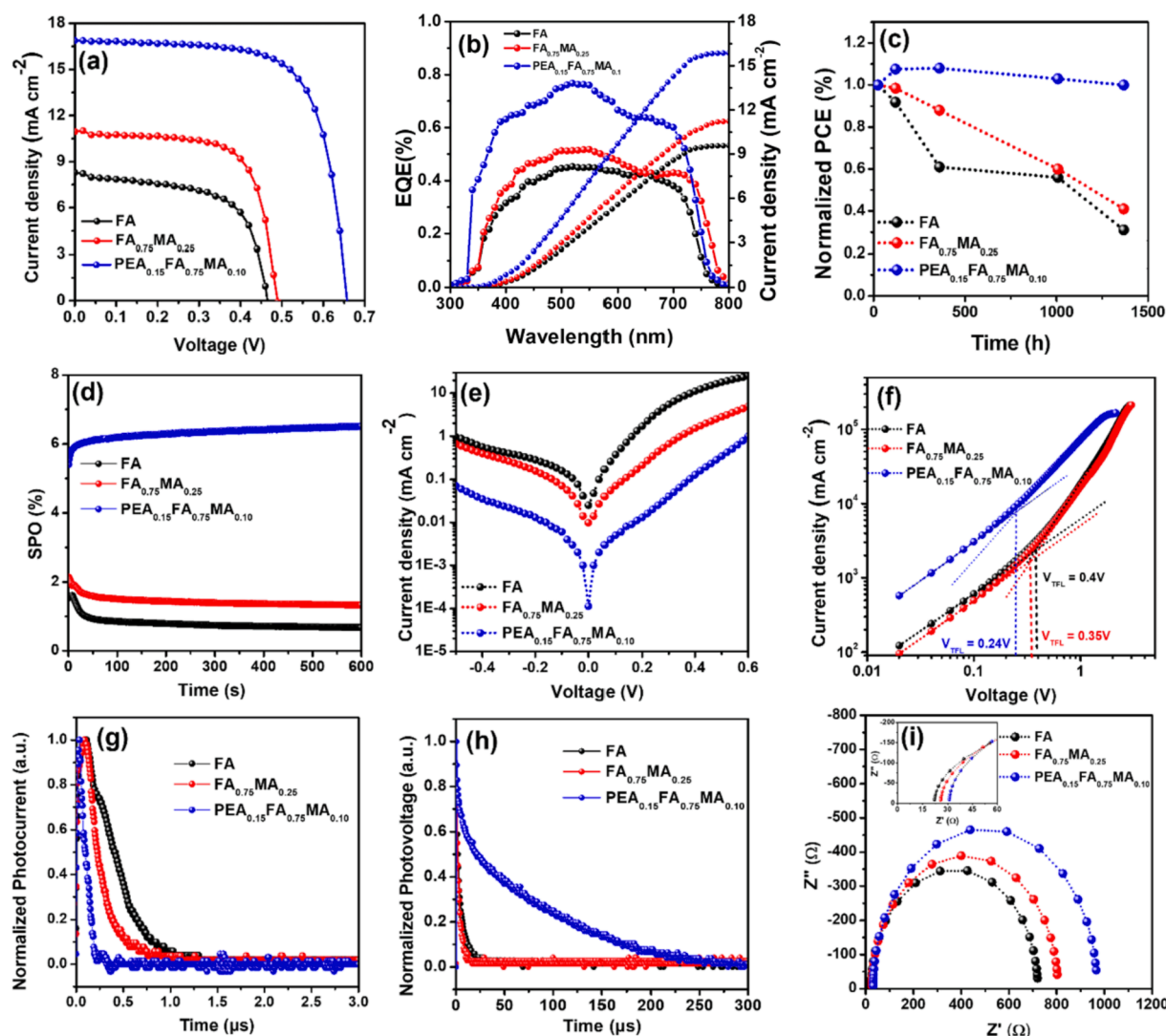


**Fig. 6.** (a) Current Density-Voltage (J-V) plots, (b) EQE spectra and the corresponding integrated  $J_{sc}$  graphs, (c) Normalized PCE graphs kept under N<sub>2</sub> atmospheric conditions without encapsulation for FA, FA<sub>0.75</sub>MA<sub>0.25</sub> and PEA<sub>0.15</sub>FA<sub>0.75</sub>MA<sub>0.10</sub> based PSCs, respectively (Device performance measured in ambient atmospheric conditions). (d) Stabilized power output at MPP for the champion device PEA<sub>0.15</sub>FA<sub>0.75</sub>MA<sub>0.10</sub> and comparative SPO graphs for FA and FA<sub>0.75</sub>MA<sub>0.25</sub>. (e) Dark J-V plots to determine leakage current and (f) Hole-only devices for measuring trap-state density for FA, FA<sub>0.75</sub>MA<sub>0.25</sub> and PEA<sub>0.15</sub>FA<sub>0.75</sub>MA<sub>0.10</sub>, respectively. (g) Transient photocurrent (TPC), (h) transient photovoltage (TPV) and (i) Nyquist plots for FA, FA<sub>0.75</sub>MA<sub>0.25</sub> and PEA<sub>0.15</sub>FA<sub>0.75</sub>MA<sub>0.10</sub>.



component, responsible for device efficiency loss. From these results we predict that precise substitution of  $\text{PEA}^+$  cation promotes highly oriented and well crystalline perovskite film with reduced surface defects.

The external quantum efficient (EQE) measurement further conducted as depicted in Fig. 6(b) in the range of 300 to 800 nm. A significant increase in the EQE with enhanced  $J_{sc}$  ( $15.87 \text{ mA}\cdot\text{cm}^{-2}$ ) for  $\text{PEA}_{0.15}\text{FA}_{0.75}\text{MA}_{0.10}$  is attributed to the better light absorption and charge collection processes [62]. Previous studies suggest that the perovskite film crystal quality plays a considerable role in mitigating non-radiative recombination losses [79]. Notably our results revealed that the substitution of  $\text{PEA}^+$  cation in 3D perovskite (i.e.,  $\text{PEA}_{0.15}\text{FA}_{0.75}\text{MA}_{0.10}$ ) significantly helped in controlling the crystal growth and led to defect passivation and trap state reduction in final film (as discussed above). On the other hand, for rest of the two cases i.e., FA and  $\text{FA}_{0.75}\text{MA}_{0.25}$ , due to the existence of defects originating through uncontrolled crystallization it resulted in severe optical losses. We may assume that the reduction in light absorption at higher wavelengths is due to geometrical losses such as reflections, scattering and waveguiding etc. [79,80]. As can be observed from the EQE graphs there is a red shift in wavelength position from FA to  $\text{FA}_{0.75}\text{MA}_{0.25}$  perovskite and further blue shift in the EQE wavelength was observed for  $\text{PEA}_{0.15}\text{FA}_{0.75}\text{MA}_{0.10}$ , that resembles well with the above findings and discussion obtained through absorbance and UPS study. It is further noted that the device PCE achieved here for the champion device ( $\text{PEA}_{0.15}\text{FA}_{0.75}\text{MA}_{0.10}$ ) is the highest performance achieved till date based on purely compositional engineering strategy. To further validate our information, we have done extensive literature review on the existing device performances achieved in various reports on WBG Sn perovskites as tabulated in Table S4.

To confirm the results as discussed in Fig. 5(a), the time dependent stability and PCE variation in device was further tested as depicted in Fig. 6(c) (stability under  $\text{N}_2$ ) and Fig. S8 (Stability in ambient atmospheric conditions). Fig. 6(c) depicts the stability comparison of devices kept in  $\text{N}_2$  filled glovebox without any encapsulation and testing was done in ambient air atmospheric conditions (i.e., under  $25^\circ\text{C}$ , R.H. of 25–30%). The normalized PCE graphs for FA and  $\text{FA}_{0.75}\text{MA}_{0.25}$  devices tend to degradation with time. However, the device fabricated with  $\text{PEA}_{0.15}\text{FA}_{0.75}\text{MA}_{0.10}$  showed excellent stability even after 1500 hrs of exposure.

PCE enhancement over the initial hours was observed in  $\text{PEA}_{0.15}\text{FA}_{0.75}\text{MA}_{0.10}$  device during stability measurement before 300 hrs completion. This spontaneous efficiency improvement relates to the self-healing phenomenon which is associated with perovskite layer homogenization and ease charge extraction and reduced recombination [81]. The initial PCE enhancement and further stabilization might be attributed to the ion movement within perovskite/transport layer interface under constant light soaking [82]. We suppose it as a general phenomenon, since the Sn based PSCs do experience the same effect as reported in previous investigations [83–85]. Though the halide ion migration is a well-established phenomenon in perovskites, however organic cation species in halide perovskites develop lattice strain or octahedral tilting within the perovskite lattice during the storage, where the organic cation in perovskite film might reorganize throughout the film results in the improvement in charge carrier extraction with reduced recombination and self-enhancement in PCEs during aging process. Hence cationic compositions in halide perovskite also plays a significant role in developing such self-enhancement in PCE [86,87], while the degradation in the device stability with time in FA and  $\text{FA}_{0.75}\text{MA}_{0.25}$  might be attributed to the high surface and bulk defects. Additionally, fresh set of devices kept under ambient atmospheric conditions to monitor the air stability of FA,  $\text{FA}_{0.75}\text{MA}_{0.25}$  and  $\text{PEA}_{0.15}\text{FA}_{0.75}\text{MA}_{0.10}$ , as the device stability with respect to time is depicted in Fig. S8. It has been observed that FA and  $\text{FA}_{0.75}\text{MA}_{0.25}$  devices under ambient atmospheric conditions tends to degradation within 5 hrs (inset Fig. S8), however  $\text{PEA}_{0.15}\text{FA}_{0.75}\text{MA}_{0.10}$  device showed long term air stability over 300 hrs, which clarifies the robustness of device and affirm that such kind of compositional engineering in WBG Sn perovskite absorber may benefit to improve overall

device performance with long term device sustainability. Fig. 6(d) represented the stabilized power output (SPO) at maximum power point (MPP) for  $\text{PEA}_{0.15}\text{FA}_{0.75}\text{MA}_{0.10}$  in comparison with FA and  $\text{FA}_{0.75}\text{MA}_{0.25}$  devices, illuminated under 1 Sun condition in ambient air. The stabilized power output measured is 6–6.5% for  $\text{PEA}_{0.15}\text{FA}_{0.75}\text{MA}_{0.10}$  near to the PCE measured from J-V characteristics for the champion device. Fig. 6(e) represents the dark J-V curves for FA,  $\text{FA}_{0.75}\text{MA}_{0.25}$  and  $\text{PEA}_{0.15}\text{FA}_{0.75}\text{MA}_{0.10}$  (Champion devices), the reverse bias J-V characteristic is lower for  $\text{PEA}_{0.15}\text{FA}_{0.75}\text{MA}_{0.10}$  as compared to FA and  $\text{FA}_{0.75}\text{MA}_{0.25}$ , suggest the minimum leakage current in  $\text{PEA}_{0.15}\text{FA}_{0.75}\text{MA}_{0.10}$  device. The above results as observed from XRD, FE-SEM and absorbance suggest that  $\text{PEA}^+$  substitution benefits to improve overall film quality and the 2D perovskite existence helps in preferentially orienting the ( $h00$ ) planes which brings high crystallinity to perovskite, collectively responsible for reduced leakage current that correlates to the suppression in trap states and non-radiative recombination [39]. We have further conducted spatial charge limit current (SCLC) measurement to determine the trap densities in perovskite films (as shown in Fig. 6(f)). The measurement was performed on ITO/PEDOT:PSS/perovskite/P3HT/Ag device and related trap densities were calculated using equation (3) from SI [88]. The calculated defect densities of FA,  $\text{FA}_{0.75}\text{MA}_{0.25}$ , and  $\text{PEA}_{0.15}\text{FA}_{0.75}\text{MA}_{0.10}$  are  $3.95 \times 10^{16} \text{ cm}^{-3}$ ,  $3.4 \times 10^{16} \text{ cm}^{-3}$ , and  $1.7 \times 10^{16} \text{ cm}^{-3}$ , respectively. These calculated results clearly indicate the suppression in trap state densities with optimal  $\text{PEA}^+$  cation substitution in WBG Sn perovskite.

Since these enhancements are related to better charge extraction and charge collection processes, transient photocurrent (TPC), transient photovoltage (TPV) and electrochemical impedance spectroscopy (EIS) measurements have been further used to unravel those enhancements in the device performances. Fig. 6(g) depicts the TPC results for FA,  $\text{FA}_{0.75}\text{MA}_{0.25}$  and  $\text{PEA}_{0.15}\text{FA}_{0.75}\text{MA}_{0.10}$  (measurement parameters and conditions are provided in SI along with the equation (4) to calculate charge-carrier lifetime and extraction time) shows that the charge carrier extraction time. For FA perovskite the charge extraction time is 3.39  $\mu\text{s}$  which further reduced to 1.98  $\mu\text{s}$  for  $\text{FA}_{0.75}\text{MA}_{0.25}$  perovskites and the minimized carrier extraction lifetime of 0.76  $\mu\text{s}$  was observed for  $\text{PEA}_{0.15}\text{FA}_{0.75}\text{MA}_{0.10}$ . In addition, TPV results in Fig. 6(h) depicts that FA and  $\text{FA}_{0.75}\text{MA}_{0.25}$  perovskite devices have larger recombination processes since the carrier lifetime 30.28  $\mu\text{s}$  and 65.57  $\mu\text{s}$  were observed for FA and  $\text{FA}_{0.75}\text{MA}_{0.25}$ , respectively, revealing the fast decay in these devices. Moreover, it has been noticed that  $\text{PEA}_{0.15}\text{FA}_{0.75}\text{MA}_{0.10}$  perovskite device experiences slower charge carrier recombination with the average carrier lifetime of 1217  $\mu\text{s}$ . These results further corroborate with the above enhanced values of  $V_{oc}$  and FF from J-V characteristic parameters of  $\text{PEA}_{0.15}\text{FA}_{0.75}\text{MA}_{0.10}$  perovskite device. Fig. 6(i) shows EIS Nyquist plots of FA,  $\text{FA}_{0.75}\text{MA}_{0.25}$ , and  $\text{PEA}_{0.15}\text{FA}_{0.75}\text{MA}_{0.10}$  devices measured in dark condition in the frequency range of 2 kHz to 1 MHz with 0.65 V applied voltage. As shown in Table S5 (SI), the EIS value shows the similar trend as for the J-V parameter. The series resistance ( $R_s$ ) values are FA,  $\text{FA}_{0.75}\text{MA}_{0.25}$  and  $\text{PEA}_{0.15}\text{FA}_{0.75}\text{MA}_{0.10}$  are 32.02, 26.01, and 18.05  $\Omega$ , respectively. These results suggest that substituting A-site cation with  $\text{PEA}^+$  helps in passivating defects in perovskite. Additionally,  $\text{PEA}_{0.15}\text{FA}_{0.75}\text{MA}_{0.10}$  perovskite has the highest recombination resistance ( $R_{rec}$ ) of 935.19  $\Omega$ , suggesting the improved  $V_{oc}$  value in device by reducing the recombination loss in perovskite. The finding in the present work is beneficial for a broad range of research as a future perspective in the direction to collectively improve the overall perovskite film uniformity with negligible pinholes, mitigate trap states, brings energy band modulations, and helps in enhancing the stability of  $\text{Sn}^{2+}$  state by compositional engineering strategy in WBG Sn perovskites and can be useful to serve as front sub-cell photo-absorbers in Pb-free all perovskite tandem devices.

### 3. Conclusion

We substituted A site cation in 3D WBG Sn perovskite with  $\text{PEA}^+$

cation, through precursor compositional engineering, which tends to the formation of 2D/3D mixed perovskite. We expect that such compositional engineering in Sn perovskites brings multiple advantages such as significant improvement in crystallinity, preferential orientation, suppressing the trap densities, improved bands alignment between perovskite and charge transport layer, efficient charge injection and reduce  $V_{oc}$  deficit, suppress moisture penetration and further oxidation of  $Sn^{2+}$  state. Furthermore, it benefits in improving the band alignments in device assembly resulted in efficient charge extraction process. Based on multiple advantages of  $PEA^+$  cation substitution to perovskite photo absorber, the champion device  $PEA_{0.15}FA_{0.75}MA_{0.10}SnI_2Br$  reached to PCE of 7.96% (with certified PCE of 7.84%) as compared to the  $FASnI_2Br$  (2.3%) and  $FA_{0.75}MA_{0.25}SnI_2Br$  (3.6%) and reported as the highest achieved PCE through compositional engineering in WBG Sn PSCs. The champion device shown to maintain almost same device performance as of initial PCE with outstanding stability of 300 hrs in air and 1500 hrs under  $N_2$  atmosphere without encapsulation. This finding provides a simplest way to achieve high PCE with enhanced stability in WBG Sn perovskites merely with compositional modifications in perovskite and can be useful as a future viewpoint in WBG Sn PSCs.

### Declaration of Competing Interest

The authors declare that they have no known competing financial interests or personal relationships that could have appeared to influence the work reported in this paper.

### Data availability

Data will be made available on request.

### Acknowledgements

This work was supported by the National Research Foundation of Korea (NRF) grant funded by the Korea government (MSIT) (NRF – 2021R1A2C4002045, 2021R1A4A2001687, and 2021K2A9A2A0800 0082).

### Appendix A. Supplementary data

Experimental details and characterizations: Perovskite precursor preparation method; perovskite solar cells fabrication; measurement techniques. FE-SEM for  $PEA^+$  cation substituted WBG Sn perovskite. Absorbance spectra and calculated bandgaps, XPS survey scan, Statistical distribution of PCEs and PCE comparison table, device performance summary related tables. Supplementary data to this article can be found online at <https://doi.org/10.1016/j.cej.2022.137388>.

### References

- I. Dincer, Renewable energy and sustainable development: a crucial review, *Renew. Sust. Energ. Rev.* 4 (2) (2000) 157–175, [https://doi.org/10.1016/S1364-0321\(99\)00011-8](https://doi.org/10.1016/S1364-0321(99)00011-8).
- A. Extnance, The reality behind solar power's next star material, *Nature* 570 (7762) (2019) 429–433, <https://doi.org/10.1038/d41586-019-01985-y>.
- R. Wang, T. Huang, J. Xue, J. Tong, K. Zhu, Y. Yang, Prospects for metal halide perovskite-based tandem solar cells, *Nat. Photonics* 15 (6) (2021) 411–425, <https://doi.org/10.1038/s41566-021-00809-8>.
- L. Lanzetta, N. Aristidou, S.A. Haque, Stability of lead and tin halide perovskites: the link between defects and degradation, *J. Phys. Chem. Lett.* 11 (2) (2020) 574–585, <https://doi.org/10.1021/acs.jpclett.9b02191>.
- J. Jeong, M. Kim, J. Seo, H. Lu, P. Ahlawat, A. Mishra, Y. Yang, M.A. Hope, F. T. Eickemeyer, M. Kim, Y.J. Yoon, I.W. Choi, B.P. Darwich, S.J. Choi, Y. Jo, J. H. Lee, B. Walker, S.M. Zakeeruddin, L. Emsley, U. Rothlisberger, A. Hagfeldt, D. S. Kim, M. Grätzel, J.Y. Kim, Pseudo-halide anion engineering for  $\alpha$ -FAPbI<sub>3</sub> perovskite solar cells, *Nature* 592 (7854) (2021) 381–385.
- K.A. Bush, K. Frohna, R. Prasanna, R.E. Beal, T. Leijtens, S.A. Swifter, M. D. McGehee, Compositional engineering for efficient wide band gap perovskites with improved stability to photoinduced phase segregation, *ACS Energy Lett.* 3 (2) (2018) 428–435, <https://doi.org/10.1021/acsenerylett.7b01255>.
- A.R.B. Mohd Yusoff, M. Vasilopoulou, D.G. Georgiadou, L.C. Palilis, A. Abate, M. K. Nazeeruddin, Passivation and process engineering approaches of halide perovskite films for high efficiency and stability perovskite solar cells, *Energy Environ. Sci.* 14 (5) (2021) 2906–2953.
- J. Werner, A. Walter, E. Rucavado, S.-J. Moon, D. Sacchetto, M. Rienecker, R. Peibst, R. Brendel, X. Niquille, S. De Wolf, P. Löper, M. Morales-Masis, S. Nicolay, B. Niesen, C. Ballif, Zinc tin oxide as high-temperature stable recombination layer for mesoscopic perovskite/silicon monolithic tandem solar cells, *Appl. Phys. Lett.* 109 (23) (2016) 233902, <https://doi.org/10.1063/1.4971361>.
- S. Albrecht, M. Saliba, J.P. Correa Baena, F. Lang, L. Kegelmann, M. Mews, L. Steier, A. Abate, J. Rappich, L. Korte, R. Schlatmann, M.K. Nazeeruddin, A. Hagfeldt, M. Grätzel, B. Rech, Monolithic perovskite/silicon-heterojunction tandem solar cells processed at low temperature, *Energy Environ. Sci.* 9 (1) (2016) 81–88.
- X. Luo, T. Wu, Y. Wang, X. Lin, H. Su, Q. Han, L. Han, Progress of all-perovskite tandem solar cells: the role of narrow-bandgap absorbers, *Sci. China Chem.* 64 (2) (2021) 218–227, <https://doi.org/10.1007/s11426-020-9870-4>.
- R. He, S. Ren, C. Chen, Z. Yi, Y.i. Luo, H. Lai, W. Wang, G. Zeng, X. Hao, Y.e. Wang, J. Zhang, C. Wang, L. Wu, F. Fu, D. Zhao, Wide-bandgap organic-inorganic hybrid and all-inorganic perovskite solar cells and their application in all-perovskite tandem solar cells, *Energy Environ. Sci.* 14 (11) (2021) 5723–5759.
- G.E. Eperon, M.T. Hörantner, H.J. Snaith, Metal halide perovskite tandem and multiple-junction photovoltaics, *Nat. Rev. Chem.* 1 (12) (2017) 1–18, <https://doi.org/10.1038/s41570-017-0095>.
- G.E. Eperon, T. Leijtens, K.A. Bush, R. Prasanna, T. Green, J.-W. Wang, D. P. McMeekin, G. Volonakis, R.L. Milot, R. May, A. Palmstrom, D.J. Slotcavage, R. A. Belisle, J.B. Patel, E.S. Parrott, R.J. Sutton, W. Ma, F. Moghadam, B. Conings, A. Babayigit, H.-G. Boyen, S. Bent, F. Giustino, L.M. Herz, M.B. Johnston, M. D. McGehee, H.J. Snaith, Perovskite-perovskite tandem photovoltaics with optimized band gaps, *Science* 354 (6314) (2016) 861–865.
- X.-G. Zhao, D. Yang, J.-C. Ren, Y. Sun, Z. Xiao, L. Zhang, Rational design of halide double perovskites for optoelectronic applications, *Joule* 2 (9) (2018) 1662–1673, <https://doi.org/10.1016/j.joule.2018.06.017>.
- T. Leijtens, K.A. Bush, R. Prasanna, M.D. McGehee, Opportunities and challenges for tandem solar cells using metal halide perovskite semiconductors, *Nat. Energy* 3 (10) (2018) 828–838, <https://doi.org/10.1038/s41560-018-0190-4>.
- M.H. Futscher, B. Ehrler, Efficiency limit of perovskite/Si tandem solar cells, *ACS Energy Lett.* 1 (4) (2016) 863–868, <https://doi.org/10.1021/acsenerylett.6b00405>.
- Z. Fang, Q. Zeng, C. Zuo, L. Zhang, H. Xiao, M. Cheng, F. Hao, Q. Bao, L. Zhang, Y. Yuan, W.-Q. Wu, D. Zhao, Y. Cheng, H. Tan, Z. Xiao, S. Yang, F. Liu, Z. Jin, J. Yan, L. Ding, Perovskite-based tandem solar cells, *Sci. Bull.* 66 (6) (2021) 621–636.
- Q. Han, Y.-T. Hsieh, L. Meng, J.-L. Wu, P. Sun, E.-P. Yao, S.-Y. Chang, S.-H. Bae, T. Kato, V. Bermudez, Y. Yang, High-performance perovskite/Cu(In, Ga)S<sub>2</sub> monolithic tandem solar cells, *Science* 361 (6405) (2018) 904–908.
- J. Li, H.-L. Cao, W.-B. Jiao, Q. Wang, M. Wei, I. Cantone, J. Lü, A. Abate, Biological impact of lead from halide perovskites reveals the risk of introducing a safe threshold, *Nat. Commun.* 11 (1) (2020) 1–5, <https://doi.org/10.1038/s41467-019-13910-y>.
- Y. Jiang, L. Qiu, E.J. Juarez-Perez, L.K. Ono, Z. Hu, Z. Liu, Z. Wu, L. Meng, Q. Wang, Y. Qi, Reduction of lead leakage from damaged lead halide perovskite solar modules using self-healing polymer-based encapsulation, *Nat. Energy* 4 (7) (2019) 585–593, <https://doi.org/10.1038/s41560-019-0406-2>.
- B. Chen, C. Fei, S. Chen, H. Gu, X. Xiao, J. Huang, Recycling lead and transparent conductors from perovskite solar modules, *Nat. Commun.* 12 (1) (2021) 1–10, <https://doi.org/10.1038/s41467-021-26121-1>.
- G. Schileo, G. Grancini, Lead or no lead? availability, toxicity, sustainability and environmental impact of lead-free perovskite solar cells, *J. Mater. Chem. C* 9 (1) (2021) 67–76, <https://doi.org/10.1039/D0TC04552G>.
- D. Zhao, Y. Yu, C. Wang, W. Liao, N. Shrestha, C.R. Grice, A.J. Cimaroli, L. Guan, R. J. Ellingson, K. Zhu, X. Zhao, R.-G. Xiong, Y. Yan, Low-bandgap mixed tin-lead iodide perovskite absorbers with long carrier lifetimes for all-perovskite tandem solar cells, *Nat. Energy* 2 (4) (2017), <https://doi.org/10.1038/nenergy.2017.18>.
- J. Tong, Z. Song, D.H. Kim, X. Chen, C. Chen, A.F. Palmstrom, P.F. Ndione, M. O. Reese, S.P. Dunfield, O.G. Reid, Carrier lifetimes of > 1  $\mu$ s in Sn-Pb perovskites enable efficient all-perovskite tandem solar cells, *Science* 364 (6439) (2019) 475–479, <https://doi.org/10.1126/science.aav7911>.
- K. Nishimura, M.A. Kamarudin, D. Hirotani, K. Hamada, Q. Shen, S. Iikubo, T. Minemoto, K. Yoshino, S. Hayase, Lead-free tin-halide perovskite solar cells with 13% efficiency, *Nano Energy* 74 (2020), 104858, <https://doi.org/10.1016/j.nanoen.2020.104858>.
- N. Sun, W. Gao, H. Dong, Y. Liu, X. Liu, Z. Wu, L. Song, C. Ran, Y. Chen, Architecture of pin Sn-based perovskite solar cells: characteristics, advances, and perspectives, *ACS Energy Lett.* 6 (8) (2021) 2863–2875, <https://doi.org/10.1021/acsenerylett.1c01170>.
- B.B. Yu, Z. Chen, Y. Zhu, Y. Wang, B. Han, G. Chen, X. Zhang, Z. Du, Z. He, Heterogeneous 2D/3D tin-halides perovskite solar cells with certified conversion efficiency breaking 14%, *Adv. Mater.* 33 (36) (2021) 2102055, <https://doi.org/10.1002/adma.202102055>.
- J.-J. Cao, Y.-H. Lou, W.-F. Yang, K.-L. Wang, Z.-H. Su, J. Chen, C.-H. Chen, C. Dong, X.-Y. Gao, Z.-K. Wang, Multifunctional potassium thiocyanate interlayer for eco-friendly tin perovskite indoor and outdoor photovoltaics, *Chem. Eng. J.* 433 (2022), 133832, <https://doi.org/10.1016/j.cej.2021.133832>.

- [29] R.E. Beal, N.Z. Hagström, J. Barrier, A. Gold-Parker, R. Prasanna, K.A. Bush, D. Passarello, L.T. Schelhas, K. Brünig, C.J. Tassone, H.-G. Steinrück, M. D. McGehee, M.F. Toney, A.F. Nogueira, Structural origins of light-induced phase segregation in organic-inorganic halide perovskite photovoltaic materials, *Matters* 2 (1) (2020) 207–219.
- [30] T. Huang, S. Tan, S. Nuryyeva, I. Yavuz, F. Babbe, Y. Zhao, M. Abdelsamie, M. H. Weber, R. Wang, K.N. Houk, C.M. Sutter-Fella, Y. Yang, Performance-limiting formation dynamics in mixed-halide perovskites, *Sci. Adv.* 7 (46) (2021), <https://doi.org/10.1126/sciadv.abj1799>.
- [31] M. Zhang, M. Lyu, J.-H. Yun, M. Noori, X. Zhou, N.A. Cooling, Q. Wang, H. Yu, P. C. Dastoor, L. Wang, Low-temperature processed solar cells with formamidinium tin halide perovskite/fullerene heterojunctions, *Nano Res.* 9 (6) (2016) 1570–1577, <https://doi.org/10.1007/s12274-016-1051-8>.
- [32] M. Chen, M.A. Kamarudin, A.K. Baranwal, G. Kapil, T.S. Ripolles, K. Nishimura, D. Hirofani, S.R. Sahamir, Z. Zhang, C. Ding, Y. Sanehira, J. Bisquet, Q. Shen, S. Hayase, High-efficiency lead-free wide band gap perovskite solar cells via guanidinium bromide incorporation, *ACS Appl. Energy Mater.* 4 (6) (2021) 5615–5624.
- [33] J. Zhang, J. Qin, T. Wu, B. Hu, Doping induced orbit-orbit interaction between excitons while enhancing photovoltaic performance in tin perovskite solar cells, *J. Phys. Chem. Lett.* 11 (17) (2020) 6996–7001, <https://doi.org/10.1021/acs.jpclett.0c01859>.
- [34] M. Chen, G. Kapil, Y. Li, M.A. Kamarudin, A.K. Baranwal, K. Nishimura, S. R. Sahamir, Y. Sanehira, H. Li, C. Ding, Z. Zhang, Q. Shen, S. Hayase, Large synergy effects of doping, a site substitution, and surface passivation in wide bandgap Pb-free  $\text{ASnI}_2\text{Br}$  perovskite solar cells on efficiency and stability enhancement, *J. Power Sources* 520 (2022) 230848, <https://doi.org/10.1016/j.jpowsour.2021.230848>.
- [35] M. Chen, G. Kapil, L. Wang, S. Razey Sahamir, A.K. Baranwal, K. Nishimura, Y. Sanehira, Z. Zhang, M. Akmal Kamarudin, Q. Shen, S. Hayase, High performance wide bandgap Lead-free perovskite solar cells by monolayer engineering, *Chem. Eng. J.* 436 (2022) 135196, <https://doi.org/10.1016/j.cej.2022.135196>.
- [36] X. Xu, K. Cao, W. Zhu, W. Gu, B. Ma, M. Qin, J. Qian, Y. Lu, Z. Liu, S. Chen, X. Lu, W. Huang, Improved crystallization and stability of mixed-cation tin iodide for lead-free perovskite solar cells, *ACS Appl. Energy Mater.* 3 (6) (2020) 5415–5426.
- [37] P. Li, H. Dong, J. Xu, J. Chen, B. Jiao, X. Hou, J. Li, Z. Wu, Ligand orientation-induced lattice robustness for highly efficient and stable tin-based perovskite solar cells, *ACS Energy Lett.* 5 (7) (2020) 2327–2334, <https://doi.org/10.1021/acsenerylett.0c00960>.
- [38] W.-G. Choi, C.-G. Park, Y. Kim, T. Moon, Sn perovskite solar cells via 2D/3D bilayer formation through a sequential vapor process, *ACS Energy Lett.* 5 (11) (2020) 3461–3467, <https://doi.org/10.1021/acsenerylett.0c01887>.
- [39] S. Shao, J. Liu, G. Portale, H.H. Fang, G.R. Blake, G.H. ten Brink, L.J.A. Koster, M. A. Loi, Highly reproducible Sn-based hybrid perovskite solar cells with 9% efficiency, *Adv. Energy Mater.* 8 (4) (2018) 1702019, <https://doi.org/10.1002/aenm.201702019>.
- [40] M. Liao, B.B. Yu, Z. Jin, W. Chen, Y. Zhu, X. Zhang, W. Yao, T. Duan, I. Djerdj, Z. He, Efficient and stable  $\text{FASnI}_3$  perovskite solar cells with effective interface modulation by low-dimensional perovskite layer, *ChemSusChem* 12 (22) (2019) 5007–5014, <https://doi.org/10.1002/cssc.201902000>.
- [41] H. Li, X. Jiang, Q. Wei, Z. Zang, M. Ma, F. Wang, W. Zhou, Z. Ning, Low-dimensional inorganic tin perovskite solar cells prepared by templated growth, *Angew. Chem. Int. Ed.* 60 (30) (2021) 16330–16336, <https://doi.org/10.1002/anie.202104958>.
- [42] M. Kim, G.-H. Kim, T.K. Lee, I.W. Choi, H.W. Choi, Y. Jo, Y.J. Yoon, J.W. Kim, J. Lee, D. Huh, H. Lee, S.K. Kwak, J.Y. Kim, D.S. Kim, Methylammonium chloride induces intermediate phase stabilization for efficient perovskite solar cells, *Joule* 3 (9) (2019) 2179–2192.
- [43] Y. Liao, H. Liu, W. Zhou, D. Yang, Y. Shang, Z. Shi, B. Li, X. Jiang, L. Zhang, L. N. Quan, R. Quintero-Bermudez, B.R. Sutherland, Q. Mi, E.H. Sargent, Z. Ning, Highly oriented low-dimensional tin halide perovskites with enhanced stability and photovoltaic performance, *J. Am. Chem. Soc.* 139 (19) (2017) 6693–6699.
- [44] S. Lee, J. Ryu, S.S. Park, S. Yoon, D.-G. Lee, J. Moon, Y.J. Kim, D.-W. Kang, A self-assembled hierarchical structure to keep the 3D crystal dimensionality in n-butylammonium cation-capped Pb-Sn perovskites, *J. Mater. Chem. A* 9 (48) (2021) 27541–27550, <https://doi.org/10.1039/D1TA06247F>.
- [45] F. Wang, X. Jiang, H. Chen, Y. Shang, H. Liu, J. Wei, W. Zhou, H. He, W. Liu, Z. Ning, 2D-quasi-2D-3D hierarchy structure for tin perovskite solar cells with enhanced efficiency and stability, *Joule* 2 (12) (2018) 2732–2743, <https://doi.org/10.1016/j.joule.2018.09.012>.
- [46] Y. Han, S. Park, C. Kim, M. Lee, I. Hwang, Phase control of quasi-2D perovskites and improved light-emitting performance by excess organic cations and nanoparticle intercalation, *Nanoscale* 11 (8) (2019) 3546–3556, <https://doi.org/10.1039/C8NR07361A>.
- [47] X. Yang, X. Zhang, J. Deng, Z. Chu, Q. Jiang, J. Meng, P. Wang, L. Zhang, Z. Yin, J. You, Efficient green light-emitting diodes based on quasi-two-dimensional composition and phase engineered perovskite with surface passivation, *Nat. Commun.* 9 (1) (2018) 1–8, <https://doi.org/10.1038/s41467-018-03702-1>.
- [48] Y. Li, J.V. Milić, A. Ummadisingu, J.-Y. Seo, J.-H. Im, H.-S. Kim, Y. Liu, M.I. Dar, S. M. Zakeeruddin, P. Wang, A. Hagfeldt, M. Grätzel, Bifunctional organic spacers for formamidinium-based hybrid D3n-Jacobson two-dimensional perovskite solar cells, *Nano Lett.* 19 (1) (2019) 150–157.
- [49] L. Lanzetta, J.M. Marin-Belouqui, I. Sanchez-Molina, D. Ding, S.A. Haque, Two-dimensional organic tin halide perovskites with tunable visible emission and their use in light-emitting devices, *ACS Energy Lett.* 2 (7) (2017) 1662–1668, <https://doi.org/10.1021/acsenerylett.7b00414>.
- [50] C.R. Kagan, D.B. Mitzi, C.D. Dimitrakopoulos, Organic-inorganic hybrid materials as semiconducting channels in thin-film field-effect transistors, *Science* 286 (5441) (1999) 945–947, <https://doi.org/10.1126/science.286.5441.945>.
- [51] Z. Zhao, F. Gu, Y. Li, W. Sun, S. Ye, H. Rao, Z. Liu, Z. Bian, C. Huang, Mixed-organic-cation tin iodide for lead-free perovskite solar cells with an efficiency of 8.12%, *Adv. Sci.* 4 (11) (2017) 1700204.
- [52] N. Pellet, P. Gao, G. Gregori, T.Y. Yang, M.K. Nazeeruddin, J. Maier, M. Grätzel, Mixed-organic-cation Perovskite photovoltaics for enhanced solar-light harvesting, *Angew. Chem.* 126 (12) (2014) 3215–3221, <https://doi.org/10.1002/ange.201309361>.
- [53] Y. Fu, M.T. Rea, J. Chen, D.J. Morrow, M.P. Hautzinger, Y. Zhao, D. Pan, L. H. Manger, J.C. Wright, R.H. Goldsmith, S. Jin, Selective stabilization and photophysical properties of metastable perovskite polymorphs of  $\text{CsPbI}_3$  in thin films, *Chem. Mater.* 29 (19) (2017) 8385–8394.
- [54] R. Quintero-Bermudez, A. Gold-Parker, A.H. Proppe, R. Munir, Z. Yang, S. O. Kelley, A. Amassian, M.F. Toney, E.H. Sargent, Compositional and orientational control in metal halide perovskites of reduced dimensionality, *Nat. Mater.* 17 (10) (2018) 900–907, <https://doi.org/10.1038/s41563-018-0154-x>.
- [55] X. Hou, S. Huang, W. Ou-Yang, L. Pan, Z. Sun, X. Chen, Constructing efficient and stable perovskite solar cells via interconnecting perovskite grains, *ACS Appl. Mater. Interfaces* 9 (40) (2017) 35200–35208, <https://doi.org/10.1021/acsami.7b08488>.
- [56] A.S. Yerramilli, Y. Chen, B. Gogoi, T. Alford, Phenyl Ethylammonium Iodide introduction into inverted triple cation perovskite solar cells for improved Voc and stability, *Org. Electron.* 93 (2021), 106121, <https://doi.org/10.1016/j.orgel.2021.106121>.
- [57] B. Chaudhary, T.M. Koh, B. Febriansyah, A. Bruno, N. Mathews, S.G. Mhaisalkar, C. Soci, Mixed-dimensional naphthylmethylammonium-methylammonium lead iodide perovskites with improved thermal stability, *Sci. Rep.* 10 (1) (2020) 1–11, <https://doi.org/10.1038/s41598-019-57015-4>.
- [58] G. Grancini, C. Roldán-Carmona, J. Zimmermann, E. Mosconi, X. Lee, D. Martineau, S. Narbey, F. Oswald, F. De Angelis, M. Graetzel, One-Year stable perovskite solar cells by 2D/3D interface engineering, *Nat. Commun.* 8 (1) (2017) 1–8, <https://doi.org/10.1038/ncomms15684>.
- [59] R.L. Milot, R.J. Sutton, G.E. Eperon, A.A. Haghighirad, J. Martinez Hardigree, L. Miranda, H.J. Snaith, M.B. Johnston, L.M. Herz, Charge-carrier dynamics in 2D hybrid metal-halide perovskites, *Nano Lett.* 16 (11) (2016) 7001–7007.
- [60] D.S. Lee, J.S. Yun, J. Kim, A.M. Soufiani, S. Chen, Y. Cho, X. Deng, J. Seidel, S. Lim, S. Huang, A.W.Y. Ho-Baillie, Passivation of grain boundaries by phenethylammonium in formamidinium-methylammonium lead halide perovskite solar cells, *ACS Energy Lett.* 3 (3) (2018) 647–654.
- [61] Q. Chen, J.-C.-R. Ke, D. Wang, M.Z. Mokhtar, A.G. Thomas, Z. Liu, Impact of halide additives on green antisolvent and high-humidity processed perovskite solar cells, *Appl. Surf. Sci.* 536 (15) (2021), 147949, <https://doi.org/10.1016/j.apsusc.2020.147949>.
- [62] S. Cho, P. Pandey, J. Park, T.-W. Lee, D.-W. Kang, Mixed solvent engineering for morphology optimization of the electron transport layer in perovskite photovoltaics, *ACS Appl. Energy Mater.* 5 (1) (2021) 387–396, <https://doi.org/10.1021/acsaem.1c02913>.
- [63] Z. Wang, Q. Lin, F.P. Chmiel, N. Sakai, L.M. Herz, H.J. Snaith, Efficient ambient-air-stable solar cells with 2D–3D heterostructured butylammonium-caesium-formamidinium lead halide perovskites, *Nat. Energy* 2 (9) (2017) 1–10, <https://doi.org/10.1038/nenergy.2017.135>.
- [64] S. Muduli, P. Pandey, G. Devatha, R. Babar, T. M. D.C. Kothari, M. Kabir, P.P. Pillai, S. Ogale, Photoluminescence quenching in self-assembled  $\text{CsPbBr}_3$  quantum dots on few-layer black phosphorus sheets, *Angew. Chem.* 130 (26) (2018) 7808–7812.
- [65] F. Li, X. Hou, Z. Wang, X. Cui, G. Xie, F. Yan, X.-Z. Zhao, Q. Tai, FA/MA cation exchange for efficient and reproducible tin-based perovskite solar cells, *ACS Appl. Mater. Interfaces* 13 (34) (2021) 40656–40663, <https://doi.org/10.1021/acsami.1c11751>.
- [66] C. Ma, N.-G. Park, Paradoxical approach with a hydrophilic passivation layer for moisture-stable, 23% efficient perovskite solar cells, *ACS Energy Lett.* 5 (10) (2020) 3268–3275, <https://doi.org/10.1021/acsenerylett.0c01848>.
- [67] J. Tong, J. Gong, M. Hu, S.K. Yadavalli, Z. Dai, F. Zhang, C. Xiao, J.I. Hao, M. Yang, M.A. Anderson, E.L. Ratcliff, J.J. Berry, N.P. Padture, Y. Zhou, K. Zhu, High-performance methylammonium-free ideal-band-gap perovskite solar cells, *Matters* 4 (4) (2021) 1365–1376.
- [68] F. Li, Y. Xie, Y. Hu, M. Long, Y. Zhang, J. Xu, M. Qin, X. Lu, M. Liu, Effects of alkyl chain length on crystal growth and oxidation process of two-dimensional tin halide perovskites, *ACS Energy Lett.* 5 (5) (2020) 1422–1429, <https://doi.org/10.1021/acsenerylett.0c00286>.
- [69] S.J. Lee, S.S. Shin, J. Im, T.K. Ahn, J.H. Noh, N.J. Jeon, S.I. Seok, J. Seo, Reducing carrier density in formamidinium tin perovskites and its beneficial effects on stability and efficiency of perovskite solar cells, *ACS Energy Lett.* 3 (1) (2017) 46–53, <https://doi.org/10.1021/acsenerylett.7b00976>.
- [70] M. Al-Mansoori, S. Al-Shaibani, A. Al-Jaedi, J. Lee, D. Choi, F.S. Hasoon, Effects of gas flow rate on the structure and elemental composition of tin oxide thin films deposited by RF sputtering, *AIP Adv.* 7 (12) (2017), 125105, <https://doi.org/10.1063/1.5001883>.
- [71] H. Yao, F. Zhou, Z. Li, Z. Ci, L. Ding, Z. Jin, Strategies for improving the stability of tin-based perovskite ( $\text{ASnX}_3$ ) solar cells, *Adv. Sci. Lett.* 7 (10) (2020) 1903540, <https://doi.org/10.1002/advs.201903540>.
- [72] P. Pandey, A. Sengupta, S. Parmar, U. Bansode, S. Gosavi, A. Swarnkar, S. Muduli, A.D. Mohite, S. Ogale,  $\text{CsPbBr}_3$ - $3\text{-Tl}_3\text{C}_2\text{x}$  MXene QD/QD heterojunction: photoluminescence quenching, charge transfer, and Cd ion sensing application,



- ACS Appl. Nano Mater. 3 (4) (2020) 3305–3314, <https://doi.org/10.1021/acsnm.0c00051>.
- [73] H. Li, X. Hao, B. Chang, Z. Li, L. Wang, L. Pan, X. Chen, L. Yin, Stiffening the Pb-X framework through a  $\pi$ -conjugated small-molecule cross-linker for high-performance inorganic CsPbI<sub>2</sub>Br perovskite solar cells, ACS Appl. Mater. Interfaces 13 (34) (2021) 40489–40501, <https://doi.org/10.1021/acsami.1c06533>.
- [74] D. Thrithamarassery Gangadharan, D. Valverde-Chávez, A.-F. Castro-Méndez, V. Prakash, R. Izquierdo, C. Silva, D. Ma, J.-P. Correa-Baena, Bulky cations improve band alignment and efficiency in Sn-Pb halide perovskite solar cells, ACS Appl. Energy Mater. 4 (3) (2021) 2616–2628.
- [75] J. Emara, T. Schnier, N. Pourdavoud, T. Riedl, K. Meerholz, S. Olthof, Impact of film stoichiometry on the ionization energy and electronic structure of CH<sub>3</sub>NH<sub>3</sub>PbI<sub>3</sub> perovskites, Adv. Mater. 28 (3) (2016) 553–559, <https://doi.org/10.1002/adma.201503406>.
- [76] M. Saliba, T. Matsui, J.-Y. Seo, K. Domanski, J.-P. Correa-Baena, M.K. Nazeeruddin, S.M. Zakeeruddin, W. Tress, A. Abate, A. Hagfeldt, M. Grätzel, Cesium-containing triple cation perovskite solar cells: improved stability, reproducibility and high efficiency, Energy Environ. Sci. 9 (6) (2016) 1989–1997.
- [77] R. Prasanna, A. Gold-Parker, T. Leijtens, B. Conings, A. Babayigit, H.-G. Boyen, M. F. Toney, M.D. McGehee, Band gap tuning via lattice contraction and octahedral tilting in perovskite materials for photovoltaics, J. Am. Chem. Soc. 139 (32) (2017) 11117–11124, <https://doi.org/10.1021/jacs.7b04981>.
- [78] C. Zhi, Z. Li, B. Wei, Recent progress in stabilizing perovskite solar cells through two-dimensional modification, APL Mater. 9 (7) (2021), 070702, <https://doi.org/10.1063/5.0056106>.
- [79] M. Rai, L.H. Wong, L. Etgar, Effect of perovskite thickness on electroluminescence and solar cell conversion efficiency, J. Phys. Chem. Lett. 11 (19) (2020) 8189–8194, <https://doi.org/10.1021/acs.jpcl.0c02363>.
- [80] P. Tockhorn, J. Sutter, R. Colom, L. Kegelman, A. Al-Ashouri, M. Roß, K. Jäger, T. Unold, S. Burger, S. Albrecht, C. Becker, Improved quantum efficiency by advanced light management in nanotextured solution-processed perovskite solar cells, ACS Photonics 7 (9) (2020) 2589–2600.
- [81] Y. Zhang, Y. Zhu, M. Hu, N. Pai, T. Qin, Y.-B. Cheng, U. Bach, A.N. Simonov, J. Lu, Self-enhancement of efficiency and self-attenuation of hysteretic behavior of perovskite solar cells with aging, J. Phys. Chem. Lett. 13 (2022) 2792–2799, <https://doi.org/10.1021/acs.jpcl.2c00278>.
- [82] A.K. Jena, A. Kulkarni, M. Ikegami, T. Miyasaka, Steady state performance, photo-induced performance degradation and their relation to transient hysteresis in perovskite solar cells, J. Power Sources 309 (2016) 1–10, <https://doi.org/10.1016/j.jpowsour.2016.01.094>.
- [83] C. Ran, W. Gao, J. Li, J. Xi, L.u. Li, J. Dai, Y. Yang, X. Gao, H. Dong, B.o. Jiao, I. Spanopoulos, C.D. Malliakas, X. Hou, M.G. Kanatzidis, Z. Wu, Conjugated organic cations enable efficient self-healing FASnI<sub>3</sub> solar cells, Joule 3 (12) (2019) 3072–3087.
- [84] E. Jokar, H.-S. Chuang, C.-H. Kuan, H.-P. Wu, C.-H. Hou, J.-J. Shyue, E. Wei-Guang Diao, Slow passivation and inverted hysteresis for hybrid tin perovskite solar cells attaining 13.5% via sequential deposition, J. Phys. Chem. Lett. 12 (41) (2021) 10106–10111.
- [85] E. Jokar, C.-H. Chien, A. Fathi, M. Rameez, Y.-H. Chang, E.-W.-G. Diao, Slow surface passivation and crystal relaxation with additives to improve device performance and durability for tin-based perovskite solar cells, Energy Environ. Sci. 11 (9) (2018) 2353–2362, <https://doi.org/10.1039/C8EE00956B>.
- [86] D.W. Ferdani, S.R. Pering, D. Ghosh, P. Kubiak, A.B. Walker, S.E. Lewis, A. L. Johnson, P.J. Baker, M.S. Islam, P.J. Cameron, Partial cation substitution reduces iodide ion transport in lead iodide perovskite solar cells, Energy Environ. Sci. 12 (7) (2019) 2264–2272, <https://doi.org/10.1039/C9EE00476A>.
- [87] H.X. Dang, K. Wang, M. Ghasemi, M.-C. Tang, M. De Bastiani, E. Aydin, E. Duzon, D. Barrit, J. Peng, D.-M. Smilgies, S. De Wolf, A. Amassian, Multi-cation synergy suppresses phase segregation in mixed-halide perovskites, Joule 3 (7) (2019) 1746–1764.
- [88] M.A. Lampert, Simplified theory of space-charge-limited currents in an insulator with traps, Phys. Rev. 103 (6) (1956) 1648, <https://doi.org/10.1103/PhysRev.103.1648>.